Author:
Gao, Bo

Title:
Particle Size Anisotropy Analysis in Single Particle Tracking using the T-Matrix Method

Particle Size Anisotropy Analysis in Single Particle Tracking using the T-Matrix Method

Bo Gao

A dissertation submitted to the University of Bristol in accordance with the requirements for award of the degree of Master of Science in the Faculty of Science, School of Physics.

September 4, 2020

word count: 16123

Abstract

This study is based on a developmental single nano-particle tracking technique SaNTA whose purpose is to extract information regarding a particle's size anisotropy including its size parameter and aspect ratio, from light scattering. The T-Matrix method has been used to establish a computational model that calculates the scattered light intensity and polarisation for a spheroidal particle undergoing Brownian motion. The validity and limitation of this model has been tested. This study analysed and simulated the relationship between particle orientation and scattered light polarisation and intensity. It gives two potential solutions for achieving SaNTA's goal - the autocorrelation function of the intensity signals detected by SaNTA and the shape of the intensity scatter plot. It indicates that increasing the viscosity can give more possibility for SaNTA to find the particle's size anisotropy information.

Acknowledgements

I want to thank the School of Physics and University of Bristol for giving me the opportunity to study physics here. I really appreciate the instruction of my supervisors, Dr Simon Hanna, and Dr Henkjan Gersen. I also want to thank Advanced Computing Research Centre for providing access to High Performance Computing platform BlueCrystal and lessons along with it. Thanks to Wil Hoffmann for the help of explaining SaNTA's geometry. Thanks to NHS for providing safe working environment during COVID-19. Thanks to Bluejeans for assistance of holding online meeting with my supervisors.

Declaration

I declare that the work in this dissertation was carried out in accordance with the requirements of the University's *Regulations and Code of Practice for Research Degree Programmes* and that it has not been submitted for any other academic award. Except where indicated by specific reference in the text, the work is the candidate's own work. Work done in collaboration with, or with the assistance of, others, is indicated as such. Any views expressed in the dissertation are those of the author.

SIGNED: ..... DATE:.....

Contents

Chapter 1

Introduction

1.1 Overview

With the development of nanoparticle tracking techniques, an instrument called size anisotropic nanoparticle tracking analysis (SaNTA) is being built. The main purpose of SaNTA is to find the size and aspect ratio parameter of a single particle by the scattered light polarisation and intensity when tracking it. It has been observed that the polarisation and intensity of scattered light signals in SaNTA is fluctuating due to the particle's Brownian translation and rotation which is highly related to the shape of the particle. However, how the light signals relate to the particle's shape is not easy to understand due to the unique geometry of SaNTA. This gives the motivation for the current project whose aim is to establish a model to extract information about the aspect ratio and size parameter of a single particle from SaNTA by simulating the scattering process and output in an typical experiment. Hopefully, the modelling can help to both tell whether it is possible to obtain these parameters from experiment and give a way of analysing data to determine them if it is possible.

The key to achieving this goal is to simulate the output from SaNTA for Brownian trajectories of different particles in different circumstances. To simulate this process, a correct Brownian motion generator and a model considering both light scattering by the particle with specific orientation and the polarisation and focusing in SaNTA's geometry is required. Thus, it is possible to obtain a sequence of intensities due to the Brownian trajectory of a given particle. This sequence will be the simulation result that represents the signals observed in experiments. Statistical and theoretical analysis on this sequence will help to establish the relationship to the particle's size and anisotropy.

In chapter 1, some basic ideas such as Brownian motion, scattering computation techniques like the T-Matrix method, SaNTA's background and geometry, etc. have been introduced. In chapter 2, the core method of realising the two parts of modelling is given, i.e., Brownian motion simulation and scattering results using the

T-Matrix method based on SaNTA's geometry. In chapter 3 some results from the simulation methodology are given along with some discussion of their significance. The first two sections of chapter 3 are mainly some verifications that compare with literature results to ensure the model is working correctly. The last section is the analysis of SaNTA's output giving by the model.

1.2 Brownian motion

1.2.1 Brownian motion: an overview

Brownian motion is the random motion of particles in a liquid resulting from collisions with fast-moving fluid molecules. This phenomenon was first discovered by Robert Brown in 1827 [1]. The motion has a pattern alternating randomly between fluctuations inside a small domain of the liquid, frequently with small jumps, and large but rare jumps to another location far away. The spectrum of the jump size, however, is continuous. See below as an example of Brownian motion for a spherical particle (Fig.1.1).

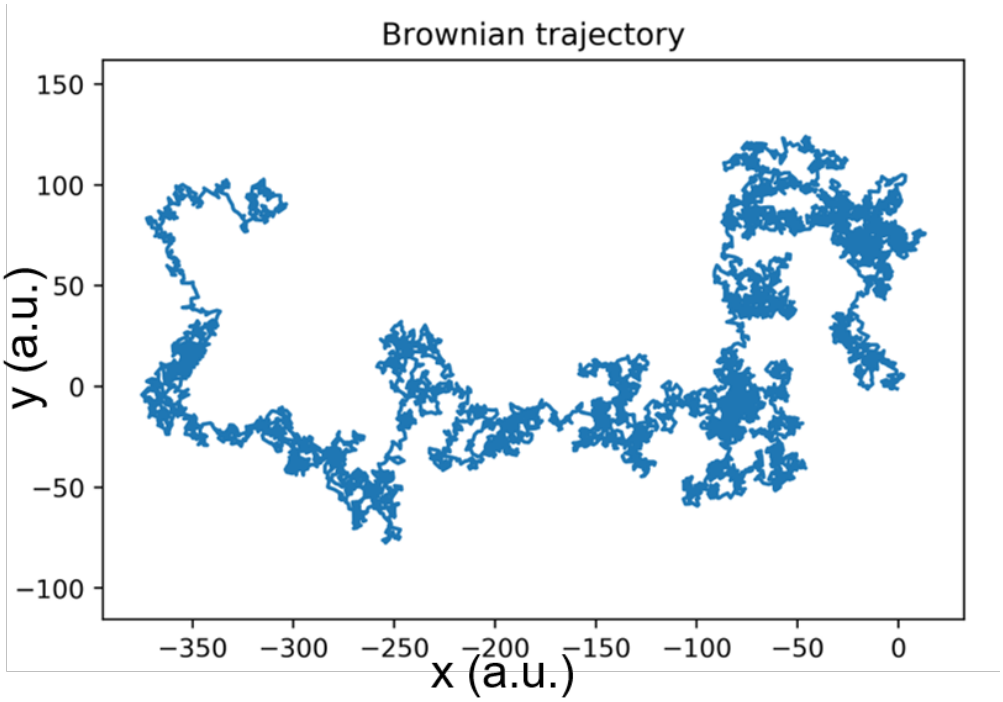

Figure 1.1: A typical trajectory of Brownian motion for a spherical particle. x and y axis are the coordinates of the particle in arbitrary units. This trajectory is simulated using diffusion coefficient $D = 1$ and time step $\delta t = 1$ for 10,000 total steps. The initial position of the particle is at coordinate $(0, 0)$.

Generally, the movement of a Brownian particle should satisfy the Langevin equation [2]:

$$\zeta \frac{\mathrm{d}}{\mathrm{d}t} \boldsymbol{r}(t) = -\boldsymbol{\nabla} U + \boldsymbol{f}(t), \tag{1.1}$$

where $\boldsymbol{r}(t)$ is the position of the particle at time t, U is the potential in space and $U = 0$ for a free particle. $\boldsymbol{\zeta}$ is called the friction tensor and its inverse $\boldsymbol{\zeta}^{-1}$ is called the mobility tensor [2], which can be obtained from hydrodynamics. For a spherical particle with radius a in a solvent with viscosity μ_0, the friction tensor is diagonal and has duplicate constant eigenvalues $\zeta = 6\pi\mu_0 a$. The diffusion coefficients can be represented as a tensor $\boldsymbol{D} = k_B T\boldsymbol{\zeta}^{-1}$, where k_B and T are the Boltzmann constant and the temperature. $\boldsymbol{f}(t)$ is the sum of random forces due to collisions between fluid molecules and the particle which is assumed to be subject to a Gaussian distribution:

$$\begin{aligned} \langle \boldsymbol{f}(t)\rangle &= 0, \\ \langle \boldsymbol{f}(t)\boldsymbol{f}(t')\rangle &= 2\boldsymbol{\zeta}k_B T\delta(t-t'), \end{aligned} \tag{1.2}$$

Therefore, the average of free particles' displacement from their initial position $\boldsymbol{r}_0$ can be calculated as:

$$\begin{aligned} \langle \boldsymbol{r}(t)\rangle &= \langle \boldsymbol{r}_0 + \boldsymbol{\zeta}^{-1}\int_0^t \mathrm{d}t'\, \boldsymbol{f}(t')\rangle \\ &= \boldsymbol{r}_0 + \boldsymbol{\zeta}^{-1}\langle \int_0^t \mathrm{d}t'\, \boldsymbol{f}(t')\rangle \\ &= \boldsymbol{r}_0 + \boldsymbol{\zeta}^{-1}\int_0^t \mathrm{d}t'\, \langle \boldsymbol{f}(t')\rangle \\ &= \boldsymbol{r}_0, \end{aligned} \tag{1.3}$$

whereas the variance of their displacements can be given by:

$$\begin{aligned} \langle \|\boldsymbol{r}(t) - \langle \boldsymbol{r}(t)\rangle\|^2\rangle &= \langle (\boldsymbol{\zeta}^{-1}\int_0^t \mathrm{d}t'\, \boldsymbol{f}(t'))(\boldsymbol{\zeta}^{-1}\int_0^t \mathrm{d}t''\, \boldsymbol{f}(t''))\rangle \\ &= (\boldsymbol{\zeta}^{-1})^2\int_0^t \mathrm{d}t' \int_0^t \mathrm{d}t''\, \langle \boldsymbol{f}(t')\boldsymbol{f}(t'')\rangle \\ &= (\boldsymbol{\zeta}^{-1})^2\int_0^t \mathrm{d}t' \int_0^t \mathrm{d}t''\, 2\boldsymbol{\zeta}k_B T\delta(t'-t'') \\ &= 2k_B T t\boldsymbol{\zeta}^{-1} \\ &= 2\boldsymbol{D}t. \end{aligned} \tag{1.4}$$

The simplest Brownian motion is the motion in one dimensional space; it is the basis of all Brownian motion studies and can be described in a statistical way with the position distribution function $\rho(x,t)$ of a large number N of particles at time t [3]:

$$\rho(x,t) = \frac{N}{\sqrt{4\pi D t}} e^{-\frac{x^2}{4Dt}}, \tag{1.5}$$

where x is the position of the particle and D is called the diffusion coefficient since

this distribution function satisfies the diffusion equation with the same coefficient:

$$\frac{\partial \rho(x,t)}{\partial t} = D\frac{\partial^2 \rho(x,t)}{\partial x^2}. \tag{1.6}$$

The distribution function is a normal (Gaussian) distribution with mean $\mu = 0$ and variance $\sigma^2 = 2Dt$. This indicates an important property of Brownian motion – the average displacement of a group of particles equals to 0 whereas the mean square of the displacement is proportional to the movement time t with a constant of $2D$. This agrees with the law of conservation of momentum as the centre of mass for a group of particles does not move. Because of this property, it is possible to characterise the Brownian motion of one particle by regarding it as a *Wiener Process*, a continuous-time stochastic process [4]. Such a process W_t (the Wiener process W at time t) can be established by following several rules:

1. $W_0 = 0$, i.e. the initial value of the process is 0.
2. The increment of the value W is independent of t.
3. $W_{t+u} - W_t \sim \mathcal{N}(0, u)$, i.e. the increment of the value is normally distributed with a mean of 0 and a variance u.
4. W_t is continuous in t.

Since for a computer it is hard to process anything related to infinitely small or infinitely large such as a continuous process, a more practical way to simulate this process is to transform the continuous Wiener Process into a discrete random walk with probability distribution function $f(x,t)$ of the displacement x at a certain time t:

$$f(x,t) = \frac{1}{\sqrt{4\pi Dt}} e^{-\frac{x^2}{4Dt}}. \tag{1.7}$$

Thus, the expectation of the particle's displacement $\langle x \rangle$ is 0 whilst the variance is given by:

$$\left\langle x^2 \right\rangle = 2Dt. \tag{1.8}$$

Notice that the expectation of moving distance $\langle |x| \rangle$, on the contrary, is not 0 but $\sqrt{2Dt}$. Therefore, the diffusion coefficient can be calculated from a long sequence of coordinates of the Brownian particle measured in experiments. The sequence can be sliced into several time intervals with equal length Δt and displacement Δx with respect to the initial position of the corresponding time interval. Then the diffusion coefficient can be calculated by:

$$D = \frac{\langle \Delta x^2 \rangle}{2\Delta t}. \tag{1.9}$$

To simulate Brownian motion, a simple but classical Monte Carlo simulation technique is typically applied. It is essential to get an accurate value of the diffusion

coefficient in advance since the movement is generated by the increment of the displacement with a normally distributed random number with mean of 0 and variance of $2Dt$. In general, the Brownian motion of an arbitrary particle can be approximated by a small sphere with appropriate diffusion coefficients if the time step is large enough and some details such as the particle's orientation can be ignored. So, the expression of the diffusion coefficient of a non-spherical particle often has the form of the coefficient of a spherical particle multiplied by a shape correction factor. This makes the understanding of the Brownian motion for a spherical particle quite important. The Brownian motion of a spherical particle can be regarded as a linear combination of two or three 1D Brownian movements with identical distributions in directions perpendicular to each other because of the symmetry of a sphere. The expression of the diffusion coefficient for a spherical particle is given by [5]:

$$D = \frac{k_B T}{6\pi\mu_0 a}, \tag{1.10}$$

where a is the radius of the spherical particle. The rotational diffusion coefficient could also be useful to describe the rotation of the particle. It has the same form as Eq. 1.9 with the angle $\Delta\theta$ of the particle rotated in a time interval Δt when measured in experiments:

$$D_\theta = \frac{\langle \Delta\theta^2 \rangle}{2\Delta t}. \tag{1.11}$$

Although the rotational Brownian motion of a spherical particle cannot be easily observed, the rotational diffusion coefficient for a spherical particle can be given by:

$$D_\theta = \frac{k_B T}{8\pi\mu_0 R^3} \tag{1.12}$$

1.2.2 Brownian motion of a spheroidal particle

The description of the Brownian motion of an asymmetrical particle can be complicated as the anisotropy of the particle and the interaction between the translational and rotational motion must be considered. Since spheroids and rods(cylinders) can constitute a first-order approximation of a wide variety of anisotropic particles, it is essential to be clear about the properties of a spheroidal particle [1].

In general, there are two ways to understand the Brownian motion of a spheroidal particle which is highly dependent on the relative time resolution when looking for its trajectory. In other words, it is related to how fast the particle moves, especially how fast it rotates. The criterion of the time resolution is called the relaxation time of rotation given by:

$$\tau_\theta = \frac{1}{2D_\theta}, \tag{1.13}$$

where D_θ is the particle's major rotational diffusion coefficient. The particle averagely rotates about $\theta \approx \sqrt{2D_\theta \Delta t}$ in time Δt and will lose the information of its

orientation when the time goes to the relaxation time, i.e. the angle should be about 1 rad (57.3°). An asymmetrical particle usually has different diffusion coefficient along each axis, and it will translate faster along the axis with higher diffusion coefficient. The trajectory observed is determined by both the translation along each axis and the particle's orientation at the moment of detection.

If the detector has time resolution much higher than the relaxation time, then the trajectory will look as if the particle tends to move along one particular direction which is the initial orientation of the particle. However, when the particle rotates fast enough or the camera is rather slow, then the trajectory will have no significant difference from a trajectory of a spherical particle, because the particle rotates so much at a single time step that it makes the decoupling of translation and rotation impossible. Therefore, calculating the diffusion coefficients along different axes and keeping the time step small is important to simulate or analyse a Brownian motion trajectory of an asymmetrical particle. For a spheroidal particle, the diffusion coefficients are given by [5–7]:

$$\begin{aligned} D_{\parallel}^{t} &= \frac{k_B T}{\mu_0 \zeta_{\parallel}^{t}}, \qquad D_{\perp}^{t} = \frac{k_B T}{\mu_0 \zeta_{\perp}^{t}}, \\ D_{\parallel}^{r} &= \frac{k_B T}{6V\mu_0 \zeta_{\parallel}^{r}}, \quad D_{\perp}^{r} = \frac{k_B T}{6V\mu_0 \zeta_{\perp}^{r}}, \end{aligned} \tag{1.14}$$

with

$$\begin{aligned} \zeta_{\parallel}^{t} &= \frac{16\pi a}{\rho^2(2\beta + \alpha_{\parallel})}, & \zeta_{\perp}^{t} &= \frac{16\pi a}{2\rho^2\beta + \alpha_{\perp}}, \\ \zeta_{\parallel}^{r} &= \frac{2}{3\alpha_{\perp}}, & \zeta_{\perp}^{r} &= \frac{2(\rho^2+1)}{3(\rho^2\alpha_{\parallel} + \alpha_{\perp})}, \\ \alpha_{\parallel} &= \frac{2}{\rho^2-1}(\rho^2\beta - 1), & \alpha_{\perp} &= \frac{\rho^2}{\rho^2-1}(1-\beta), \\ \beta &= \frac{\cosh^{-1}\rho}{\rho\sqrt{\rho^2-1}}, \quad (\rho > 1), \\ \beta &= \frac{\cos^{-1}\rho}{\rho\sqrt{1-\rho^2}}, \quad (\rho < 1), \end{aligned} \tag{1.15}$$

where $V = \frac{4}{3}\pi a b^2$ is the volume of the spheroid (see Fig. 1.2 for definition of a spheroid), ζ is the corresponding element of the friction tensor, and $\rho = a/b$ is the corresponding aspect ratio. Here, a and b are the length of the major and minor axes of the ellipsoid. The particle is a prolate spheroid when $\rho > 1$ and an oblate spheroid when $\rho < 1$. $D_{\parallel}^{t}$ and $D_{\perp}^{t}$ denote the translational motion parallel and perpendicular to the major axis respectively, whereas the superscript r denotes the rotational motion about the corresponding axis (the axis parallel or perpendicular to the major axis). Notice that the two directions perpendicular to the major axis have the same diffusion coefficients. When the particle is reduced to a sphere ($a = b$), the aspect ratio ρ will take the value of 1, then $\zeta_{\parallel}^{t} = \zeta_{\perp}^{t} = 6\pi a$ and $\zeta_{\parallel}^{r} = \zeta_{\perp}^{r} = 1$. The

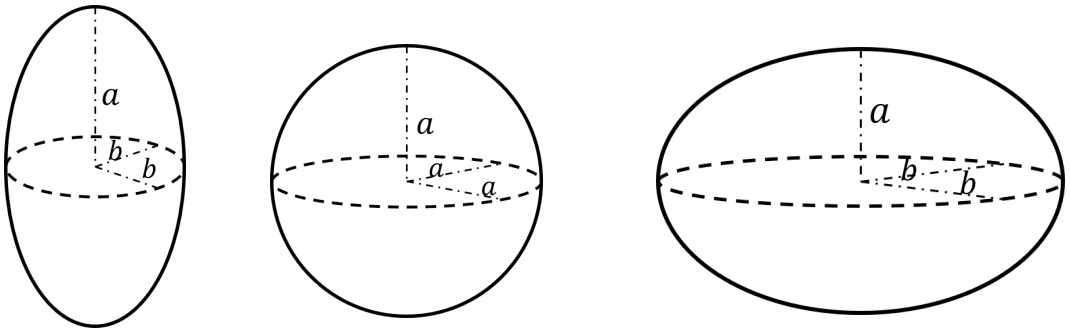

(a) Prolate spheroid ($a > b$)

(b) Sphere

(c) Oblate spheroid ($a < b$)

Figure 1.2: Definition of a spheroid.

overall displacement can be given by multiplying the direction cosine of the particle's orientation and corresponding displacement along particle's axis (see details in section 3.1.1). On the other hand, when the time step is large enough with respect to the relaxation time, there is no need to keep track of the particle's orientation and its translation in each axis. The trajectory can be generated by a spherical particle with equivalent diffusion coefficients. For the translational coefficient, it is the average over all the axes and given by [8]:

$$\begin{aligned} D &= \frac{k_B T}{6\pi\mu_0 a} G(\rho), \\ D_\theta &= \frac{k_B T}{8\pi\mu_0 a^3} [\frac{3}{2} \frac{(2\rho^2 - 1)G(\rho) - \rho^2}{\rho^2 - 1/\rho^2}] \end{aligned} \tag{1.16}$$

where $G(\rho)$ is a shape-dependent factor for the particle. For a spheroidal particle, the shape factor is given by:

$$\begin{aligned} G(\rho) &= \frac{\rho \ln\left(\rho + \sqrt{\rho^2 - 1}\right)}{\sqrt{\rho^2 - 1}} = \frac{\rho \cosh^{-1} \rho}{\sqrt{\rho^2 - 1}}, \ (\rho > 1) \\ G(\rho) &= \frac{\rho \tan^{-1}(\sqrt{1 - \rho^2}/\rho)}{\sqrt{1 - \rho^2}} = \frac{\rho \cos^{-1} \rho}{\sqrt{1 - \rho^2}}, \ (\rho < 1) \end{aligned} \tag{1.17}$$

1.3 Light Scattering

Light scattering is a common optical phenomenon and it reflects properties of both scatterer and incident light. There are two classes of problems that draw a great amount of interest - the direct problem and the inverse problem. The direct problem is to calculate theoretically or to observe experimentally the scattering by a known and well-defined system. The inverse problem is to characterise the system from a knowledge of the scattering, usually obtained by experiment or from observations of natural phenomena [9]. To better solve the inverse problem, or to better characterise the scattering system, a suitable theoretical model describing the scattering process

needs to be adopted.

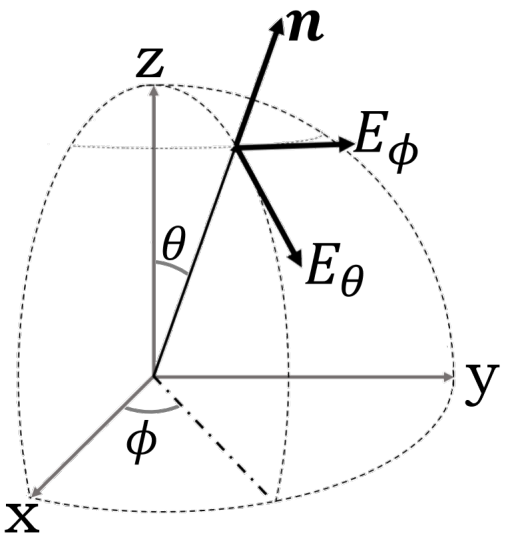

Figure 1.3: Polarisation components notation for a given light beam. $\boldsymbol{n}$ is the wave vector of the light beam, which can be described by angular coordinates (θ, ϕ) in spherical coordinates system. E_θ and E_ϕ are basis vectors for the electric field for the light beam, which gives the vertical and horizontal polarisation components, respectively.

When considering a monochromatic plane electromagnetic wave as the incident light beam in a direction $\boldsymbol{n}^{inc}$, its time independent part of electric vector can be given by [10]:

$$\begin{aligned}\boldsymbol{E}^{inc}(\boldsymbol{R}) &= (E_{\theta 0}^{inc}\hat{\boldsymbol{\theta}}^{inc} + E_{\phi 0}^{inc}\hat{\boldsymbol{\phi}}^{inc})\exp\big(ik\boldsymbol{n}^{inc}\cdot\boldsymbol{R}\big) = \boldsymbol{E}_0^{inc}\exp\big(ik\boldsymbol{n}^{inc}\cdot\boldsymbol{R}\big) \\ &= E_\theta^{inc}\hat{\boldsymbol{\theta}}^{inc} + E_\phi^{inc}\hat{\boldsymbol{\phi}}^{inc}\end{aligned} \tag{1.18}$$

where $k = 2\pi/\lambda$ is the wavenumber, and λ is the wavelength, $\boldsymbol{R}$ is the radius vector in laboratory coordinate system. The subscript θ and ϕ of electric vectors are defined in Fig.1.3. Because of the linearity of Maxwell's equations and boundary condition, the expression for the scattered electric field should be linearly related to the incident electric field. Hence, the time factor $\exp(-i\omega t)$ can be ignored. In the far-field region ($kR \gg 1, R = |\boldsymbol{R}|$), the scattered wave becomes spherical and is given by [11]:

$$\boldsymbol{E}^{sca}(\boldsymbol{R}) = E_\theta^{sca}(R, \boldsymbol{n}^{sca})\hat{\boldsymbol{\theta}}^{sca} + E_\phi^{sca}(R, \boldsymbol{n}^{sca})\hat{\boldsymbol{\phi}}^{sca} \tag{1.19}$$

where $\boldsymbol{n}^{sca} = \frac{\boldsymbol{R}}{R}$ is the scattered light direction. Obviously, the scattered electric vector is perpendicular to the radius vector $\boldsymbol{R}$:

$$\boldsymbol{R}\cdot\boldsymbol{E}^{sca}(\boldsymbol{R}) = 0 \tag{1.20}$$

The 2×2 amplitude matrix $\boldsymbol{S}$ can be introduced to represent the linear trans-

formation from incident light to scattered light:

$$\begin{bmatrix} E_\theta^{sca} \\ E_\phi^{sca} \end{bmatrix} = \frac{e^{ikR}}{R} \boldsymbol{S}(\boldsymbol{n}^{inc}, \boldsymbol{n}^{sca}; \alpha, \beta, \phi) \begin{bmatrix} E_\theta^{inc} \\ E_\phi^{inc} \end{bmatrix} \tag{1.21}$$

where α, β, γ are Euler angles to represent the orientation of the particle (see details in Sec.2.1.2).

Since photometric and polarimetric optical instruments cannot measure the electric field of a light beam directly but rather some quantities that are quadratic combinations of the electric field components, the Stokes parameters to describe the status of a monochromatic transverse electromagnetic wave are introduced [10, 12]:

$$\boldsymbol{I} = \begin{bmatrix} I \\ Q \\ U \\ V \end{bmatrix} \tag{1.22}$$

with

$$\begin{aligned} I &= E_\theta \overline{E_\theta} + E_\phi \overline{E_\phi}, \\ Q &= E_\theta \overline{E_\theta} - E_\phi \overline{E_\phi}, \\ U &= -E_\theta \overline{E_\phi} - E_\phi \overline{E_\theta}, \\ V &= i(E_\phi \overline{E_\theta} - E_\theta \overline{E_\phi}), \end{aligned} \tag{1.23}$$

where the overline denotes the complex conjugate value. The component I is the irradiance of the beam, and Q and U describe the linear polarisation state whereas V describe the circular polarisation state. As follows from the definition of Stokes parameters, for an elementary monochromatic plane wave or spherical wave, the identity should hold:

$$I^2 = Q^2 + U^2 + V^2 \tag{1.24}$$

However, if the light beams are incoherent mixtures of several elementary waves, as they usually will be, the identity will be replaced by the inequality [10, 11]:

$$I^2 \geq Q^2 + U^2 + V^2 \tag{1.25}$$

The degree of polarisation p can be introduced as:

$$p = \frac{\sqrt{Q^2 + U^2 + V^2}}{I} \leq 1 \tag{1.26}$$

whereas the ratios $\sqrt{Q^2 + U^2}/I$ and V/I are called degree of linear and circular polarisation, respectively. Based on the definition of Stokes parameters and the

amplitude matrix, the 4×4 phase matrix $\boldsymbol{Z}$ can be introduced:

$$\boldsymbol{I}^{sca} = \frac{1}{R^2}\boldsymbol{Z}(\boldsymbol{n}^{inc}, \boldsymbol{n}^{sca}; \alpha, \beta, \phi)\boldsymbol{I}^{inc} \tag{1.27}$$

Therefore, finding the expression for the amplitude matrix or the phase matrix will help a lot when trying to solve scattering problems. However, both matrices rely on not only the properties of scatterer and incident light but also the direction of observation, i.e., the matrices should be calculated over and over again either when the observation direction is changed or the orientation and shape of the scatterer are changed. This is inconvenient since the computation of these matrices could be extremely expensive, especially when the particle is anisotropic and large. To fix this problem, many methods have been developed for different kinds of approximations.

1.3.1 Rayleigh Scattering

Rayleigh scattering theory describes the scattering by small dielectric particle. When the particle is small enough compared to the wavelength and is illuminated by a linear polarised light beam, it becomes polarised in the electromagnetic field and the instantaneous field it experiences is uniform over its extent. Rayleigh scattering theory regards the scattered light as the electromagnetic radiation of the dipole moment induced by the electric field inside the particle.

For a spherical particle with radius of a, the induced dipole moment $\boldsymbol{p}$ under an external electric field $\boldsymbol{E_0}$ can be given by [13]:

$$\boldsymbol{p} = 4\pi\epsilon_2 a^3 \frac{\epsilon_1 - \epsilon_2}{\epsilon_1 + 2\epsilon_2}\boldsymbol{E_0} \tag{1.28}$$

where ϵ_1 and ϵ_2 are the dielectric permittivities capacities of the sphere and the external medium, respectively. The polarisability α' can be introduced as part of the factor preceding $\boldsymbol{E_0}$:

$$\alpha' = a^3 \frac{\epsilon_1 - \epsilon_2}{\epsilon_1 + 2\epsilon_2} \tag{1.29}$$

Therefore, for an incident wave of unit intensity, the intensity of the scattered wave at a distance r from the particle is given by [14]:

$$I = \frac{16\pi^4 a^6}{r^2\lambda^4}\left(\frac{\epsilon_1 - \epsilon_2}{\epsilon_1 + 2\epsilon_2}\right)^2 \sin^2\psi \tag{1.30}$$

or

$$I = \frac{16\pi^4 a^6}{r^2\lambda^4}\left|\frac{n^2 - 1}{n^2 + 2}\right|^2 \sin^2\psi \tag{1.31}$$

where n is the relative refractive index of the particle. It can be replaced by the complex refractive index m if the particle is weak absorptive. ψ is the angle measured from the scattering direction to the dipole, i.e. the direction of electric vector of incident light for spherical particle.

When dealing with non-spherical particles, it would be helpful to replace the constant polarisability by a tensor $\boldsymbol{\alpha}$ since the polarisability along different axes could be different. Then the induced dipole moment could be expressed as:

$$\boldsymbol{p} = 4\pi\epsilon_2\boldsymbol{\alpha}\boldsymbol{E_0} \tag{1.32}$$

The polarisability tensor is usually diagonal when the lab-frame is identical to the particle-frame, and its expression is different from Eq.1.29:

$$\alpha_i = \frac{V(m^2-1)}{4\pi + (m^2-1)P_i} \tag{1.33}$$

where V is the volume of the particle and P_i is the depolarisation factor along the i-th axis. The exact expression of the depolarisation factor P is decided by the shape of the particle. For example, the expression of an ellipsoidal particle with three axes length a_1, a_2 and a_3 can be given by [15]:

$$P_i = \int_0^\infty \mathrm{d}s \ \frac{2\pi}{s+a_i}\prod_{j=1}^{3}\frac{1}{\sqrt{s+a_j}} \tag{1.34}$$

Rayleigh scattering is under the limit of small particles, i.e., for a spherical particle with radius a, it should satisfy $a/\lambda \ll 0.05$. Therefore, it is important to keep an eye on the radius when dealing with scattering by nanoparticles as a light beam with wavelength of 500nm requires the particle to be much smaller than 25nm and even smaller when the particle is asymmetric.

1.3.2 T-Matrix Method

Since Rayleigh Scattering is not always suitable when dealing with scattering by nanoparticles, a more compatible method needs to be adopted. The T-Matrix method is a powerful approach in this realm as it can calculate scattering by any-shape any-size particles theoretically. The basic idea of the T-Matrix method is to expand incident and scattered waves in infinite series of vector spherical wave functions (VSWFs) [16]:

$$\begin{aligned}
\boldsymbol{E}^{inc}(\boldsymbol{R}) &= \sum_{n=1}^{\infty}\sum_{m=-n}^{n}[a_{mn}\mathrm{Rg}\boldsymbol{M}_{mn}(k\boldsymbol{R}) + b_{mn}\mathrm{Rg}\boldsymbol{N}_{mn}(k\boldsymbol{R})], \\
\boldsymbol{E}^{sca}(\boldsymbol{R}) &= \sum_{n=1}^{\infty}\sum_{m=-n}^{n}[p_{mn}\boldsymbol{M}_{mn}(k\boldsymbol{R}) + q_{mn}\boldsymbol{N}_{mn}(k\boldsymbol{R})], \ R > R_>
\end{aligned} \tag{1.35}$$

where $R_>$ denotes the radius of the smallest circumscribed sphere, and

$$\begin{aligned}
\boldsymbol{M}_{mn}(k\boldsymbol{R}) &= (-1)^m d_n h_n^{(1)}(kR)\boldsymbol{C}_{mn}(\theta,\phi) \\
\mathrm{Rg}\boldsymbol{M}_{mn}(k\boldsymbol{R}) &= (-1)^m d_n j_n(kR)\boldsymbol{C}_{mn}(\theta,\phi) \\
\boldsymbol{N}_{mn}(k\boldsymbol{R}) &= (-1)^m d_n \{\frac{n(n+1)}{kR} h_n^{(1)}(kR)\boldsymbol{P}_{mn}(\theta,\phi) \\
&\quad + \frac{1}{kR}[kRh_n^{(1)}(kR)]'\boldsymbol{B}_{mn}(\theta,\phi)\} \\
\mathrm{Rg}\boldsymbol{N}_{mn}(k\boldsymbol{R}) &= (-1)^m d_n \{\frac{n(n+1)}{kR} j_n(kR)\boldsymbol{P}_{mn}(\theta,\phi) \\
&\quad + \frac{1}{kR}[kRj_n(kR)]'\boldsymbol{B}_{mn}(\theta,\phi)\}
\end{aligned} \tag{1.36}$$

with

$$d_n = \sqrt{\frac{2n+1}{4\pi n(n+1)}} \tag{1.37}$$

$\boldsymbol{P}_{mn}(\theta,\phi)$, $\boldsymbol{B}_{mn}(\theta,\phi)$ and $\boldsymbol{C}_{mn}(\theta,\phi)$ are the so-called vector spherical wave functions since they are vector forms of the spherical harmonic function [11]:

$$\begin{aligned}
\boldsymbol{P}_{mn}(\theta,\phi) &= \hat{\boldsymbol{R}} Y_n^m(\theta,\phi) \\
\boldsymbol{B}_{mn}(\theta,\phi) &= R\boldsymbol{\nabla}(Y_n^m(\theta,\phi)) \\
&= (\hat{\boldsymbol{\theta}}\frac{\mathrm{d}P_n^m(\cos\theta)}{\mathrm{d}\theta} + \hat{\boldsymbol{\phi}}\frac{im}{\sin\theta}P_n^m(\cos\theta))e^{im\phi} \\
&= \hat{\boldsymbol{R}} \times \boldsymbol{C}_{mn}(\theta,\phi) \\
\boldsymbol{C}_{mn}(\theta,\phi) &= \boldsymbol{\nabla} \times (\boldsymbol{R}Y_n^m(\theta,\phi)) \\
&= (\hat{\boldsymbol{\theta}}\frac{im}{\sin\theta}P_n^m(\cos\theta) - \hat{\boldsymbol{\phi}}\frac{\mathrm{d}P_n^m(\cos\theta)}{\mathrm{d}\theta})e^{im\phi}
\end{aligned} \tag{1.38}$$

where $\hat{\boldsymbol{R}}, \hat{\boldsymbol{\theta}}, \hat{\boldsymbol{\phi}}$ are the three basis vectors of spherical coordinate system, $P_n^m(x)$ is the associated Legendre polynomial defined as [17]:

$$P_n^m = \frac{(-1)^m}{2^n n!}(1-x^2)^{m/2}\frac{\mathrm{d}^{n+m}}{\mathrm{d}x^{n+m}}\big((x^2-1)^n\big) \tag{1.39}$$

and $Y_n^m(\theta,\phi)$ is the spherical harmonic function defined by:

$$Y_n^m(\theta,\phi) = P_n^m(\cos\theta)e^{im\phi} \tag{1.40}$$

Obviously, the T-Matrix method cannot deal with the scattered field too close to the particle properly when $R < R_>$.

The expansion coefficients of the plane incident wave are given by the following simple analytical formulas [11]:

$$\begin{aligned}
a_{mn} &= 4\pi(-1)^m i^n d_n \overline{\boldsymbol{C}_{mn}(\theta^{inc})}\boldsymbol{E}_0^{inc}\exp\big(-im\phi^{inc}\big) \\
b_{mn} &= 4\pi(-1)^m i^n d_n \overline{\boldsymbol{B}_{mn}(\theta^{inc})}\boldsymbol{E}_0^{inc}\exp\big(-im\phi^{inc}\big)
\end{aligned} \tag{1.41}$$

Owing to the linearity of Maxwell's equations and boundary conditions, the relation between the scattered field coefficients p_{mn} and q_{mn} and the incident field coefficients a_{mn} and b_{mn} must be linear and is given by a transition matrix (the T-Matrix) $\boldsymbol{T}$ [11]:

$$\begin{aligned} p_{mn} &= \sum_{n'=1}^{\infty} \sum_{m'=-n'}^{n'} [T^{11}_{mnm'n'} a_{m'n'} + T^{12}_{mnm'n'} b_{m'n'}] \\ q_{mn} &= \sum_{n'=1}^{\infty} \sum_{m'=-n'}^{n'} [T^{21}_{mnm'n'} a_{m'n'} + T^{22}_{mnm'n'} b_{m'n'}] \end{aligned} \tag{1.42}$$

In compact matrix notation, it can be rewritten as:

$$\begin{bmatrix} \boldsymbol{p} \\ \boldsymbol{q} \end{bmatrix} = \boldsymbol{T} \begin{bmatrix} \boldsymbol{a} \\ \boldsymbol{b} \end{bmatrix} = \begin{bmatrix} \boldsymbol{T}^{11} & \boldsymbol{T}^{12} \\ \boldsymbol{T}^{21} & \boldsymbol{T}^{22} \end{bmatrix} \begin{bmatrix} \boldsymbol{a} \\ \boldsymbol{b} \end{bmatrix} \tag{1.43}$$

Therefore, if the T-matrix of a given scatterer is known, based on Eq.1.35, Eq.1.41 and Eq.1.43, the expressions for the scattered field can be calculated. Also, for far field scattering the amplitude matrix $\boldsymbol{S}$ can be given by [16]:

$$\begin{aligned} \boldsymbol{S}(\boldsymbol{n}^{inc}, \boldsymbol{n}^{sca}) = \frac{4\pi}{k} \sum_{nmn'm'} & i^{n'-n'1} d_n d_{n'} \exp\big[i(m\phi^{sca} - m'\phi^{inc})\big] \\ & \times \{[T^{11}_{mnm'n'} \boldsymbol{C}_{mn}(\theta^{sca}) + T^{21}_{mnm'n'} i\boldsymbol{B}_{mn}(\theta^{sca})]\overline{\boldsymbol{C}_{m'n'}(\theta^{inc})} \\ & + [T^{21}_{mnm'n'} \boldsymbol{C}_{mn}(\theta^{sca}) + T^{22}_{mnm'n'} i\boldsymbol{B}_{mn}(\theta^{sca})]\overline{\boldsymbol{B}_{m'n'}(\theta^{inc})}/i\} \end{aligned} \tag{1.44}$$

A fundamental feature of the T-matrix approach is that the T-matrix depends only on the physical and geometrical characteristics of the scattering particle (refractive index, size, shape, and orientation with respect to the reference frame). [16] Thus, the scattering problem can be solved in an object-oriented way, i.e., separate it into three parts - the incident field, the scatterer, and the scattered field. The first two parts can be altered independently, and the third part gives the result of scattering with arbitrary direction.

The expression for the T-matrix can be given by several surface integrals over the particle and some matrix operations [11]. First, let

$$\begin{bmatrix} J^{(11)}_{mnm'n'} \\ J^{(12)}_{mnm'n'} \\ J^{(21)}_{mnm'n'} \\ J^{(22)}_{mnm'n'} \end{bmatrix} = (-1)^m \int_S \mathrm{d}\boldsymbol{S} \cdot \begin{bmatrix} \mathrm{Rg}\boldsymbol{M}_{m'n'}(k_s\boldsymbol{R}) \times \boldsymbol{M}_{-mn}(k\boldsymbol{R}) \\ \mathrm{Rg}\boldsymbol{M}_{m'n'}(k_s\boldsymbol{R}) \times \boldsymbol{N}_{-mn}(k\boldsymbol{R}) \\ \mathrm{Rg}\boldsymbol{N}_{m'n'}(k_s\boldsymbol{R}) \times \boldsymbol{M}_{-mn}(k\boldsymbol{R}) \\ \mathrm{Rg}\boldsymbol{N}_{m'n'}(k_s\boldsymbol{R}) \times \boldsymbol{N}_{-mn}(k\boldsymbol{R}) \end{bmatrix} \tag{1.45}$$

and

$$\begin{aligned} P_{mnm'n'} &= -ikk_s J^{(21)}_{mnm'n'} - ik^2 J^{(12)}_{mnm'n'} \\ R_{mnm'n'} &= -ikk_s J^{(11)}_{mnm'n'} - ik^2 J^{(22)}_{mnm'n'} \\ S_{mnm'n'} &= -ikk_s J^{(22)}_{mnm'n'} - ik^2 J^{(11)}_{mnm'n'} \\ U_{mnm'n'} &= -ikk_s J^{(12)}_{mnm'n'} - ik^2 J^{(21)}_{mnm'n'} \end{aligned} \tag{1.46}$$

where k_s is the wave number of the scattered light just in case it is different form the incident light. Then define the matrices:

$$\begin{aligned} \boldsymbol{Q} &= \begin{bmatrix} \boldsymbol{P} & \boldsymbol{R} \\ \boldsymbol{S} & \boldsymbol{U} \end{bmatrix} \\ \mathrm{Rg}\boldsymbol{Q} &= \begin{bmatrix} \mathrm{Rg}\boldsymbol{P} & \mathrm{Rg}\boldsymbol{R} \\ \mathrm{Rg}\boldsymbol{S} & \mathrm{Rg}\boldsymbol{U} \end{bmatrix} \end{aligned} \tag{1.47}$$

where Rg means replace $\boldsymbol{M}_{-mn}$ and $\boldsymbol{N}_{-mn}$ terms in the integral by $\mathrm{Rg}\boldsymbol{M}_{-mn}$ and $\mathrm{Rg}\boldsymbol{N}_{-mn}$ respectively. The T-matrix can finally be given by:

$$\boldsymbol{T} = -\mathrm{Rg}\boldsymbol{Q}\ \boldsymbol{Q}^{-1} \tag{1.48}$$

Another benefit of using the T-matrix is that once the T-matrix is obtained, there is no need to recalculate the surface integral again if the shape of the particle does not change, especially if the particle is rotated. The change of the T-matrix can be calculated by multiplying the representation of the rotation group $D^{(n)}_{m'm}(\alpha\beta\gamma)$ with spherical harmonic functions as basis [11]:

$$D^{(n)}_{m'm}(\alpha\beta\gamma) = e^{im'\gamma} d^{(n)}_{m'm}(\beta) e^{im\alpha} \tag{1.49}$$

with

$$\begin{aligned} d^{(n)}_{m'm}(\beta) = &\sqrt{\frac{(j+m')!(j-m')!}{(j+m)!(j-m)!}} (\cos\frac{\beta}{2})^{m'+m} \\ &\times (\sin\frac{\beta}{2})^{m'-m} P^{(m'-m,m'+m)}_{j-m'}(\cos\beta) \end{aligned} \tag{1.50}$$

where $P^{(a,b)}_n(x)$ is the Jacobi polynomial of order n and degree (a,b) [17].

Although theoretically the T-matrix can deal with a particle with any-shape and any-size, since the computer has limitations handling infinitely small or infinitely large, the T-matrix method requires a cut off number of terms to speed up the calculation under certain accuracy. Generally, a particle with higher size parameter or higher size anisotropy needs more VSWF terms and more terms for generating the mesh of the surface integral.

1.4 Nanoparticle Tracking Analysis

Nanoparticle Tracking Analysis (NTA) is a technique that can provide direct and real-time visualisation, sizing and counting of nanoparticles between 10nm and 1μm in liquid suspension [18]. Generally, the methodology of NTA (see Fig.1.4) is to observe the light signal scattered by the Brownian moving nanoparticles when they encounter the incident laser beam, which forms an image of various light spots. The positions of these light spots will move around and can be tracked by a certain algorithm, which gives NTA the ability to do single particle tracking. Therefore NTA also provides a kind of direct observation of particles' Brownian motion. Due to the properties of Brownian motion mentioned in Section 1.2.1, NTA is a very good way to characterise the particle size distribution.

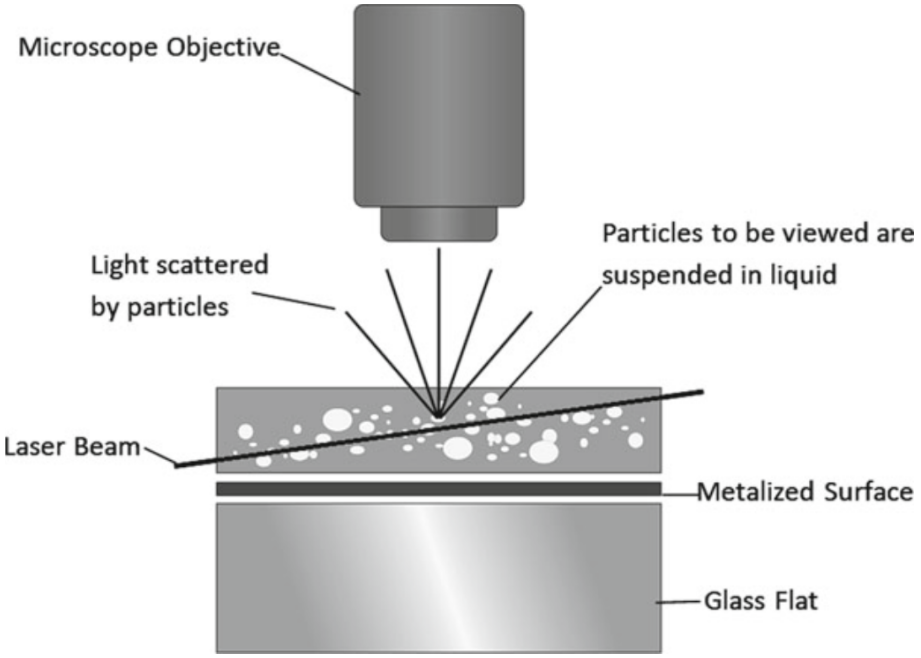

Figure 1.4: Methodology of NTA

NTA is not only a fast single particle tracking technique, because it can track many nanoparticles at the same time. This means it can also analyse the concentration, high resolution particle size distribution, and even the particle's fluorescent properties and dynamic properties under a motive force [19]. Benefiting from these abilities, NTA is widely applied in a variety of areas especially in biophysics such as drug delivery and targeting [20], protein aggregation [21] and virus counting [22], etc.

1.5 Single Particle Orientation and Rotational Tracking

While NTA is focused on the translational motion of particles, the Single Particle Orientation and Rotational Tracking (SPORT) technique aims to explore the

additional dimension of rotation for anisotropic nanoparticles [23].

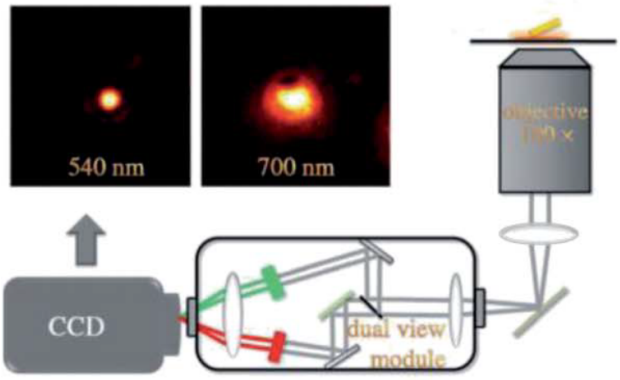

(a) Dual wavelength view module [23, 24]

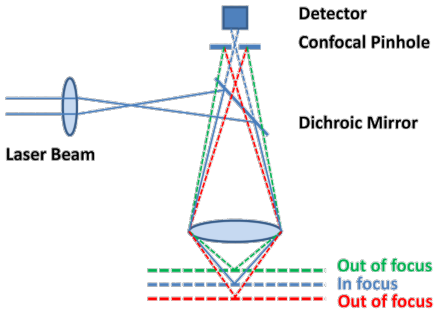

(b) Dual wavelength system mechanism [24]

Figure 1.5: SPORT mechanism, reprint from [23, 24]

Although SPORT is a newly developed technique (2010) [25], it has been applied in several studies such as rotational behaviour of F_1-ATP Synthase, nanoparticle diffusion on membranes, cargo transport by molecular motors, etc [23]. This technique uses the dual wavelength view module (see Fig.1.5a) to analyse the orientation and rotation of a particle with given size parameter and aspect ratio [23, 24]. The main mechanism of the dual wavelength system is that light with different wavelengths are focused at different positions by a lens (see Fig.1.5b). As shown in Fig.1.5a, the focused 540nm light (bright field) is to locate the nanoparticle and the defocused 700nm light (dark field) is to give the orientation information when compared with the 540nm light spot [23, 24]. It has been shown that SPORT works well for 2D rotation as the angle ϕ adopts $\arccos^4$ and $\arcsin^4$ relationship with the normalised light intensity signal I/I_{max} for dark field and bright field respectively [23, 25].

1.6 Dynamic Light Scattering

Another technique that can be compared with NTA is Dynamic Light Scattering (DLS), also known as *photon-correlation spectroscopy*, or *quasi-elastic light scattering*, which is often used to measure the dynamics of molecules in condensed systems by studying the scattered light intensity fluctuations or frequency distribution. [26] Unlike NTA, DLS is not a single particle analysis technique but provides an average over a large number of particles.

A photon correlation technique is commonly used in DLS, whose key is to study the correlation function $G(\tau)$ of the light signal $I(t)$:

$$G(\tau) = \lim_{T\to\infty} \frac{1}{2T} \int_{-T}^{T} I(t)I(t+\tau)\,\mathrm{d}t. \tag{1.51}$$

The correlation function is both experimentally accessible and theoretically inter-

pretable since it can be measured by designed digital techniques and it is actually the Fourier transform of the power spectrum of the fluctuation (this comes from the properties of the Fourier transform of a convolution). [27] For example, the spectrum for the translational diffusion of a mono-disperse molecule is a Lorentzian:

$$P(\omega) = \frac{2Dq^2/\pi}{\omega^2 + (2Dq^2)^2}, \tag{1.52}$$

where q is the magnitude of the wave vector of the density fluctuations giving rise to the scattering [28], which is related to the wavelength of light in the medium λ and the scattered angle θ:

$$q = \frac{4\pi}{\lambda} \sin\left(\frac{\theta}{2}\right). \tag{1.53}$$

D is the diffusion coefficient given by Eq.1.10. And the correlation function will be:

$$G(\tau) = 1 + e^{-2Dq^2\tau}. \tag{1.54}$$

A general DLS process can be described as scattering with geometry given by Fig.1.6. There are two typical cases that are worth looking at for small particles. Most scattering experiments in this project can be described as a combination of these two cases.

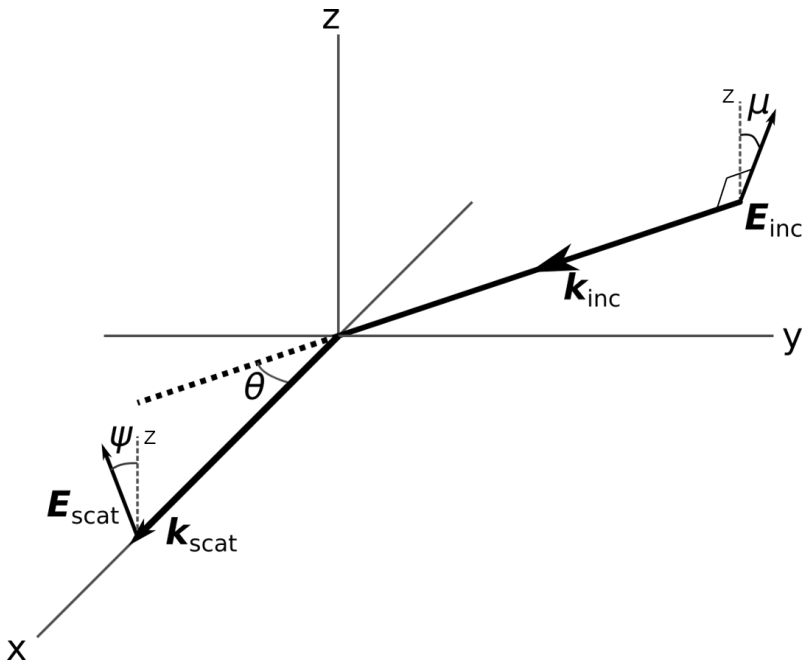

Figure 1.6: Scattering geometry. $\boldsymbol{k}_{inc}$ and $\boldsymbol{k}_{scat}$ are the wave vectors of the incident and scattered light respectively. $\boldsymbol{E}_{inc}$ and $\boldsymbol{E}_{inc}$ are the corresponding polarisation vectors with angle μ and ψ refer to the z axis. θ is the scattering angle.

The first case is when $\mu = 0°$ and $\psi = 0°$, which is also known as Polarised Dynamic Light Scattering (PDLS). [29] When the particle is a small sphere, which can be regarded as a perfect dipole, the scattered light will be linearly polarised

with the same polarisation as the incident light. Therefore, PDLS is a good way to characterise how similar the particle is with respect to the incident light direction. The autocorrelation function (ACF) of the scattered light intensity $G_{VV}(t)$ (the subscript VV refers to *Vertical to Vertical*) is given by [29, 30]:

$$G_{VV}(t) = A[e^{-q^2Dt}]^2 + B, \tag{1.55}$$

where q is the magnitude of scattering vector given by Eq.1.53, D is the translational diffusion coefficient of the particle. A and B are constants for a given q and incident light intensity, they can be set to 1 and 0 respectively if the ACF is normalised, i.e. it equals to 1 at $t = 0$ and tends to 0 when t goes to infinity.

The other case is when $\mu = 0°$ and $\psi = 90°$, which can be known as Depolarised Dynamic Light Scattering (DDLS). This is particularly important when dealing with the particle's size/optical anisotropy [29, 30] since the intensity of DDLS should always be 0 when the particle is isotropic. The ACF of the intensity of DDLS $G_{VH}(t)$ (the subscript VH refers to *Vertical to Horizontal*) is given by:

$$G_{VH}(t) = A[e^{-(q^2D+6D_\theta)t}]^2 + B, \tag{1.56}$$

where q and D is the same as in Eq.1.55, A and B are constants and can be set to 1 and 0 when the ACF is normalised. D_θ is the rotational diffusion coefficient of the particle. The diffusion coefficients are given by Eq.1.16.

There is another important case which can be described with $\mu = 90°$ and $\psi = 90°$ denoted as *Horizontal-Horizontal* scattering. It is useful when dealing with large structures [29, 31] which is not mainly focused on in this project. Thus, this case will not be deeply discussed here.

1.7 Size anisotropic Nanoparticle Tracking Analysis

As mentioned above, conventional NTA technique is a single particle-based analysis method and it can profile the size parameter of a selected nanoparticle. However, it is unable to tell the difference between size anisotropic nanoparticles with similar sizes but different aspect ratios. It is possible for DLS to calculate the aspect ratio distribution for a group of nanoparticles by exponential fitting the ACF and solving Eq.1.55 and Eq.1.56. But it is not a single particle-based method, i.e., it cannot make characterisation for a single particle directly, which is unideal especially in complex systems. As for SPORT, it can visualise the orientation and rotational behaviour for in-plane rotation (azimuthal angle), but has faced some difficulties for out-plane rotation (polar or elevation angle) when resolving 3D rotation of a nanorod [23].

Size anisotropic Nanoparticle Tracking Analysis (SaNTA) is a technique currently

under development aiming to extract the size parameter and aspect ratio information of a single nanoparticle by studying its rotational behaviour. Considering the properties of PDLS and DDLS, it would be possible to solve for size parameter and aspect ratio if proper polarisation channels are added to the conventional NTA technique. The original thought is to use only one camera for signal processing like SPORT. In this case, the polariser needs to be rotated by 45° to have significant signal in both channels as the DDLS is too small compared to PDLS when the particle's aspect ratio is not big enough. Then it turns out that it would be more convenient to use two cameras instead of one since the particle should always be in the same position for both channels.

As shown in Fig.1.7, SaNTA's geometry can be divided into three parts. The incident part controls the polarisation state of incident light such that the beam is linearly polarised in the y-direction. The scattering part is where the scattering process happens. The detector part includes lenses to collect scattered light and the polarising beam splitter (PBS) to separate it into two channels with polarisations perpendicular to each other. The detector part can be rotated about the z-axis to change bases for scattered light polarisation. When the direction of the detector part is shown as in the figure, one channel is looking at PPLS and the other is looking at DPLS. Another choice of direction is to rotate the detector part by 45°, then the two channels are looking at DPLS+PPLS (plus channel) and DPLS-PPLS (minus channel) which is convenient when looking for the polarisation difference caused by particle's size anisotropy.

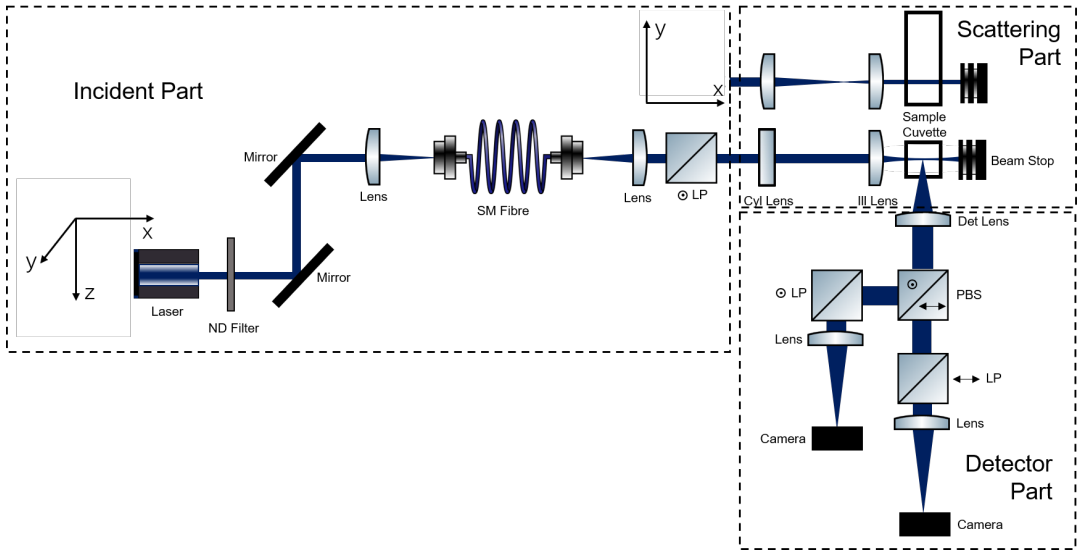

Figure 1.7: Optical path diagram of SaNTA. LP - Linear polariser; Cyl Lens - Cylindrical lens; Ill Lens - Illumination lens; Det Lens - Detection lens

Chapter 2

Methods

2.1 Brownian motion simulation

2.1.1 2D Brownian motion generator

The Brownian motion generator can always be treated as an iteration of the particle's position and orientation changed by some random kick characterised by a few independent random numbers. The status of the particle at time t_n only relies on its status at time t_{n-1}. All the Brownian motion simulation is programmed using *Python*, the random number is generated by functions in the package *numpy*.

Since orientation and rotation for spherical particles in 2D space can be ignored, only the degree of freedom for translation (x, y) is considered. Because of the isotropy of a sphere, the random kick $(\delta x, \delta y)$ will be generated by two independent random numbers with the same distribution function, i.e., a normal distribution with mean of 0 and standard deviation (std.) of $\sqrt{2D\delta t}$, where D is the diffusion coefficient of a sphere given by Eq.1.10 and δt is the time step given by the simulation set up. The geometry of this part is given by Fig.2.1a

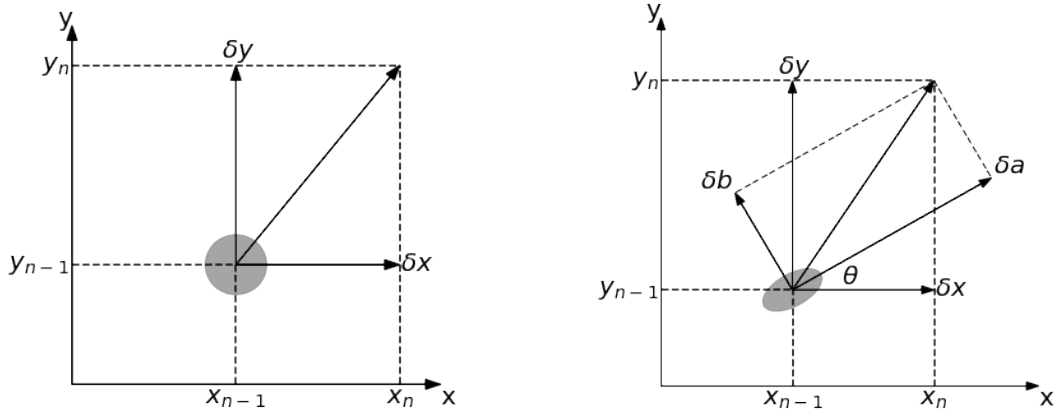

(a) Geometry set up for 2D spherical particle Brownian motion.

(b) Geometry set up for 2D spheroidal particle Brownian motion.

Figure 2.1: (a) The position for sphere at time t_n,(x_n, y_n) can be calculated by $x_n = \delta x + x_{n-1}, y_n = \delta y + y_{n-1}$. (b) θ denotes the angle between the particle's symmetric axis and the x-axis in lab-frame.

As for a spheroidal particle in 2D space, its orientation must be considered when the time step δt is much smaller than the relaxation time $\tau = \frac{1}{2D_\theta}$, where D_θ is the main rotational diffusion coefficient given by $D_\perp^r$ in Eq.1.14. Due to the coupling of translation and rotation, the probability distribution of the random kick in the lab-frame $(\delta x, \delta y)$ is no longer the simple normal distribution, while the random kick in the body-frame $(\delta a, \delta b)$ is normally distributed with both mean of 0 and std. of $\sqrt{2D_a\delta t}$ and $\sqrt{2D_b\delta t}$ respectively. D_a and D_b here are the translational diffusion coefficients in the body-frame given by $D_\parallel^t$ and $D_\perp^t$ in Eq.1.14. The random kick in the lab-frame $(\delta x, \delta y)$ can be converted from the kick in the body-frame $(\delta a, \delta b)$ by the coordinate system rotation matrix $\boldsymbol{R}$:

$$\begin{aligned} \boldsymbol{R} &= \begin{bmatrix} \cos\theta & -\sin\theta \\ \sin\theta & \cos\theta \end{bmatrix} \\ \begin{bmatrix} \delta x \\ \delta y \end{bmatrix} = \boldsymbol{R} \begin{bmatrix} \delta a \\ \delta b \end{bmatrix} &= \begin{bmatrix} \cos\theta & -\sin\theta \\ \sin\theta & \cos\theta \end{bmatrix} \begin{bmatrix} \delta a \\ \delta b \end{bmatrix} \end{aligned} \tag{2.1}$$

where θ describes the current orientation of the particle (see Fig.2.1b for geometry set up). With the rotation matrix $\boldsymbol{R}$ given by Eq.2.1, the position (x_n, y_n) at time t_n can be calculated from the position at time t_{n-1} using $x_n = \delta x + x_{n-1}, y_n = \delta y + y_{n-1}$. The orientation at time t_n, on the other hand, can also be calculated from the orientation at time t_{n-1} by $\theta_n = \delta\theta + \theta_{n-1}$, where $\delta\theta$ is the rotation random kick or the step rotation, which can be given by a normally distributed random number with mean of 0 and std. of $\sqrt{2D_\theta\delta t}$. Notice that the angle θ here is in radians unit.

2.1.2 3D Brownian motion generator

Although the 2D free Brownian motion can be easily simulated and analysed, it is nearly impossible to find an actual free particle moving in a 2D plane. There will always be confinements for a 2D Brownian motion, whose interaction with particle shall greatly influence the expression of diffusion coefficients. Thus, the behaviour of the particle in a 2D plane could be very different from that in a 3D space. Since there is no confinement for the particle in SaNTA's geometry, use of the 3D Brownian motion generator instead of refinement of the diffusion coefficient expressions is required.

One additional coordinate should be included when describing the 3D spherical particle trajectory compared to 2D. However, 6 degrees of freedom $(x, y, z; \alpha, \beta, \gamma)$ are needed to characterise an anisotropic particle in general, where (α, β, γ) represent the orientation of the particle. (see Fig.2.2 for notation) Similar to the 2D spheroid case in Section 2.1.1, the 3D Brownian motion can be simulated by gaussian kicks of translation and rotation in the body-frame, converted into the lab-frame by coordinate system transformation. The traditional way is to denote the orientation by

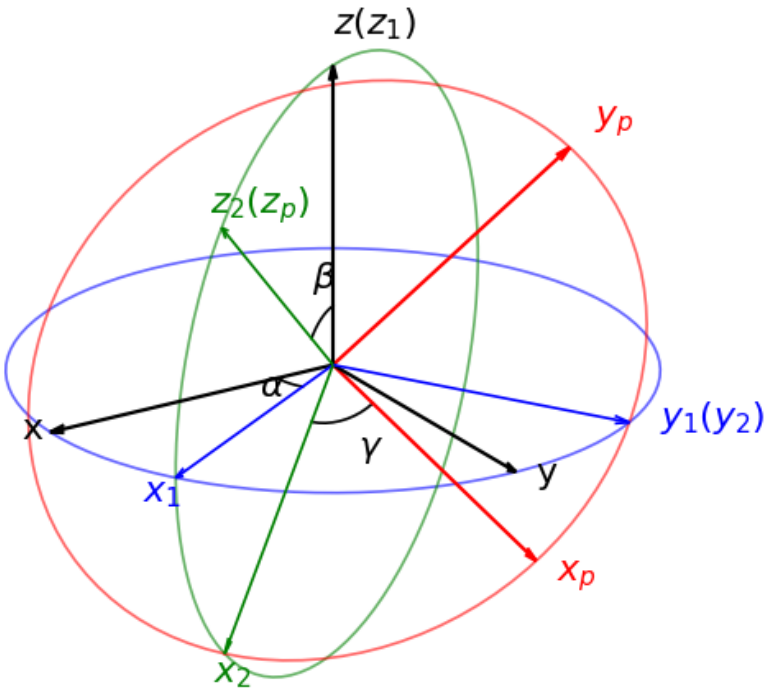

Figure 2.2: 'ZYZ' Euler angle geometry.

Euler angles in the *ZYZ* convention, and to do the transformation by the *Direction Cosine Matrix* (DCM) as follows:

1) Establish lab-frame by xyz system as black arrows shown in Fig 2.2. Rotate lab-frame xyz about z-axis by angle $\alpha \in [0, 2\pi)$ and construct the $x_1y_1z_1$ system (blue arrows). Any vector $\boldsymbol{v}$ in the new system can be transformed into xyz system by using the DCM $\boldsymbol{D_1}(\alpha)$:

$$\boldsymbol{D_1}(\alpha) = \begin{bmatrix} \cos\alpha & \sin\alpha & 0 \\ -\sin\alpha & \cos\alpha & 0 \\ 0 & 0 & 1 \end{bmatrix} \tag{2.2}$$

and

$$\begin{bmatrix} v_x^1 & v_y^1 & v_z^1 \end{bmatrix} \begin{bmatrix} x_1 \\ y_1 \\ z_1 \end{bmatrix} = \begin{bmatrix} v_x^1 & v_y^1 & v_z^1 \end{bmatrix} \boldsymbol{D_1}(\alpha) \begin{bmatrix} x \\ y \\ z \end{bmatrix} = \begin{bmatrix} v_x & v_y & v_z \end{bmatrix} \begin{bmatrix} x \\ y \\ z \end{bmatrix} \tag{2.3}$$

where $\begin{bmatrix} x_1 \\ y_1 \\ z_1 \end{bmatrix}$ is the basis vector of the $x_1y_1z_1$ system given by:

$$\begin{bmatrix} x_1 \\ y_1 \\ z_1 \end{bmatrix} = \boldsymbol{D_1}(\alpha) \begin{bmatrix} x \\ y \\ z \end{bmatrix} \tag{2.4}$$

2) Rotate the $x_1y_1z_1$ system about y_1-axis by angle $\beta \in [0, \pi]$ and obtain the

$x_2y_2z_2$ system (green arrows). Similarly, vector $\boldsymbol{v}$ can be transformed into the $x_1y_1z_1$ system by DCM $\boldsymbol{D_2}(\beta)$:

$$\boldsymbol{D_2}(\beta) = \begin{bmatrix} \cos\beta & 0 & -\sin\beta \\ 0 & 1 & 0 \\ \sin\beta & 0 & \cos\beta \end{bmatrix} \tag{2.5}$$

and

$$\begin{bmatrix} v_x^2 & v_y^2 & v_z^2 \end{bmatrix} \begin{bmatrix} x_2 \\ y_2 \\ z_2 \end{bmatrix} = \begin{bmatrix} v_x^2 & v_y^2 & v_z^2 \end{bmatrix} \boldsymbol{D_2}(\beta) \begin{bmatrix} x_1 \\ y_1 \\ z_1 \end{bmatrix} = \begin{bmatrix} v_x & v_y & v_z \end{bmatrix} \begin{bmatrix} x \\ y \\ z \end{bmatrix} \tag{2.6}$$

where $\begin{bmatrix} x_2 \\ y_2 \\ z_2 \end{bmatrix}$ is the basis vector of the $x_2y_2z_2$ system given by:

$$\begin{bmatrix} x_2 \\ y_2 \\ z_2 \end{bmatrix} = \boldsymbol{D_2}(\beta) \begin{bmatrix} x_1 \\ y_1 \\ z_1 \end{bmatrix} \tag{2.7}$$

3) Rotate the $x_2y_2z_2$ system about z_2-axis by angle $\gamma \in [0, 2\pi)$ and establish the body-frame $x_py_pz_p$ system (red arrows). Vector $\boldsymbol{v}$ can be transformed into the $x_2y_2z_2$ system by DCM $\boldsymbol{D_3}(\gamma)$:

$$\boldsymbol{D_3}(\gamma) = \begin{bmatrix} \cos\gamma & \sin\gamma & 0 \\ -\sin\gamma & \cos\gamma & 0 \\ 0 & 0 & 1 \end{bmatrix} \tag{2.8}$$

and

$$\begin{bmatrix} v_x^p & v_y^p & v_z^p \end{bmatrix} \begin{bmatrix} x_p \\ y_p \\ z_p \end{bmatrix} = \begin{bmatrix} v_x^p & v_y^p & v_z^p \end{bmatrix} \boldsymbol{D_3}(\gamma) \begin{bmatrix} x_2 \\ y_2 \\ z_2 \end{bmatrix} = \begin{bmatrix} v_x & v_y & v_z \end{bmatrix} \begin{bmatrix} x \\ y \\ z \end{bmatrix} \tag{2.9}$$

where $\begin{bmatrix} x_p \\ y_p \\ z_p \end{bmatrix}$ is the basis vector of the $x_py_pz_p$ system given by:

$$\begin{bmatrix} x_p \\ y_p \\ z_p \end{bmatrix} = \boldsymbol{D_3}(\gamma) \begin{bmatrix} x_2 \\ y_2 \\ z_2 \end{bmatrix} \tag{2.10}$$

Therefore, the expression of total DCM of body-frame $\boldsymbol{D}(\alpha, \beta, \gamma)$ and the trans-

formation can be given by:

$$\begin{aligned}\boldsymbol{D}(\alpha,\beta,\gamma) &= \boldsymbol{D_3}(\gamma)\boldsymbol{D_2}(\beta)\boldsymbol{D_1}(\alpha)\\ &= \begin{bmatrix}\cos\gamma & \sin\gamma & 0\\ -\sin\gamma & \cos\gamma & 0\\ 0 & 0 & 1\end{bmatrix}\begin{bmatrix}\cos\beta & 0 & -\sin\beta\\ 0 & 1 & 0\\ \sin\beta & 0 & \cos\beta\end{bmatrix}\begin{bmatrix}\cos\alpha & \sin\alpha & 0\\ -\sin\alpha & \cos\alpha & 0\\ 0 & 0 & 1\end{bmatrix}\end{aligned} \tag{2.11}$$

$$= \begin{bmatrix}\cos\gamma\cos\beta\cos\alpha - \sin\gamma\sin\alpha & \cos\gamma\cos\beta\sin\alpha + \sin\gamma\cos\alpha & -\cos\gamma\sin\beta\\ -\sin\gamma\cos\beta\cos\alpha - \cos\gamma\sin\alpha & -\sin\gamma\cos\beta\sin\alpha + \cos\gamma\cos\alpha & \sin\gamma\sin\beta\\ \sin\beta\cos\alpha & \sin\beta\sin\alpha & \cos\beta\end{bmatrix}$$

and

$$\begin{aligned}\begin{bmatrix}x_p\\ y_p\\ z_p\end{bmatrix} &= \boldsymbol{D}(\alpha,\beta,\gamma)\begin{bmatrix}x\\ y\\ z\end{bmatrix}\\ \begin{bmatrix}v_x^p & v_y^p & v_z^p\end{bmatrix}\begin{bmatrix}x_p\\ y_p\\ z_p\end{bmatrix} &= \begin{bmatrix}v_x^p & v_y^p & v_z^p\end{bmatrix}\boldsymbol{D}(\alpha,\beta,\gamma)\begin{bmatrix}x\\ y\\ z\end{bmatrix}\\ &= \begin{bmatrix}v_x & v_y & v_z\end{bmatrix}\begin{bmatrix}x\\ y\\ z\end{bmatrix}\end{aligned} \tag{2.12}$$

An advantage of using the ZYZ conventional Euler angle is that the spherical angular coordinates (θ,ϕ) (polar and azimuthal angle respectively) for the z_p-axis of body-frame $x_py_pz_p$, which usually denotes the symmetric axis for the spheroid, is the same as the Euler angle (β,α)

If the particle at time t_{n-1} is at position $(x_{n-1},y_{n-1},z_{n-1})$ with orientation described by the Euler angle $(\alpha_{n-1},\beta_{n-1},\gamma_{n-1})$, then the position and orientation at time t_n will be calculated by 6 corresponding random kicks $(\delta a,\delta b_1,\delta b_2,\delta\alpha,\delta\beta,\delta\gamma)$, where δa and $\delta b_1,\delta b_2$ are step displacement along the major axis and two minor axes while $\delta\alpha,\delta\beta,\delta\gamma$ are Euler angles of body-frame at time t_n compared to time t_{n-1}. All these random kicks can be given by normal random number with mean of 0 and corresponding std. from Eq.1.14.

According to Eq.2.11, the total DCM that transforms the body-frame at time t_n and t_{n-1} to the lab-frame can be given by $\boldsymbol{D_n} = \boldsymbol{D}(\alpha_n,\beta_n,\gamma_n)$ and $\boldsymbol{D_{n-1}} = \boldsymbol{D}(\alpha_{n-1},\beta_{n-1},\gamma_{n-1})$ while the DCM of the orientation random kick can be given by $\boldsymbol{\delta_D} = \boldsymbol{D}(\delta\alpha,\delta\beta,\delta\gamma)$. The expression of Euler angle $(\alpha_n,\beta_n,\gamma_n)$ can be found by solving the equation:

$$\boldsymbol{D}(\alpha_n,\beta_n,\gamma_n) = \boldsymbol{D_n} = \boldsymbol{\delta_D}\boldsymbol{D_{n-1}}, \tag{2.13}$$

which can be derived from Eq.2.12:

$$\begin{aligned} \begin{bmatrix} x_{n-1} \\ y_{n-1} \\ z_{n-1} \end{bmatrix} &= \boldsymbol{D_{n-1}} \begin{bmatrix} x \\ y \\ z \end{bmatrix} \\ \begin{bmatrix} x_n \\ y_n \\ z_n \end{bmatrix} = \boldsymbol{\delta_D} \begin{bmatrix} x_{n-1} \\ y_{n-1} \\ z_{n-1} \end{bmatrix} &= \boldsymbol{\delta_D D_{n-1}} \begin{bmatrix} x \\ y \\ z \end{bmatrix} = \boldsymbol{D_n} \begin{bmatrix} x \\ y \\ z \end{bmatrix} \end{aligned} \tag{2.14}$$

Use the transformation for the body-frame displacement $(\delta a, \delta b_1, \delta b_2)$ in Eq.2.12 to get the lab-frame displacement $(\delta x, \delta y, \delta z)$:

$$\begin{bmatrix} \delta x & \delta y & \delta z \end{bmatrix} \begin{bmatrix} x \\ y \\ z \end{bmatrix} = \begin{bmatrix} \delta a & \delta b_1 & \delta b_2 \end{bmatrix} \begin{bmatrix} x_p \\ y_p \\ z_p \end{bmatrix} = \begin{bmatrix} \delta a & \delta b_1 & \delta b_2 \end{bmatrix} \boldsymbol{D_n} \begin{bmatrix} x \\ y \\ z \end{bmatrix} \tag{2.15}$$

which gives the expression of lab-frame displacement vector $\begin{bmatrix} \delta x \\ \delta y \\ \delta z \end{bmatrix}$ by the Rotation Matrix or the transpose of the DCM ($\boldsymbol{D_n^T}$):

$$\begin{bmatrix} \delta x \\ \delta y \\ \delta z \end{bmatrix} = \boldsymbol{D_n^T} \begin{bmatrix} \delta a \\ \delta b_1 \\ \delta b_2 \end{bmatrix} \tag{2.16}$$

2.2 Scattering model construction

The core of this part is to calculate the correct scattering results of a spheroidal particle with given orientation. This can be achieved by using the T-Matrix method. The T-Matrix is only related to the particle's shape and is independent of the particle's orientation and the incident light. Thus, it is only necessary to multiply by an additional rotation matrix of the particle instead of recalculating the whole T-Matrix when the particle rotates. Although the T-Matrix is usually computed in vector spherical wave function (VSWF) representation, it would be more convenient if it can be converted into the scattering amplitude matrix, because the incident light is linear polarised plane wave in SaNTA's geometry. The T-Matrix and corresponding amplitude matrix $\boldsymbol{S}(\boldsymbol{n_{inc}}, \boldsymbol{n_{sca}}; \alpha, \beta, \gamma)$ is computed by a *Fortran77* software provided by Mishchenko [32–35] and a *Python* package called *pytmatrix* that interfaces the *Fortran* code with *Python* [36]. To explore the validity and limitations of this package, several result comparisons have been made including theoretical results for T-Matrix components of a small spherical particle and Mie scattering of certain spheroids given in the literature by solving Maxwell's equations in spheroidal coordinate system [37].

In computation, the direction of the x-axis of the lab-frame is set as the inci-

dent beam direction and the z-axis is set as the optical axis in the detector part (see Fig1.7). The relationship between scattered light and incident light and the amplitude matrix $\boldsymbol{S}$ is described by Eq.1.21. Since the incident light in SaNTA is horizontally polarised (along y-axis), then the vertical component of incident light E_θ^{inc} will always be 0 and the E_ϕ^{inc} component can be regarded as a constant E_0 (see Fig1.3 for definition of E_θ and E_ϕ components). Meanwhile, the Euler angle γ will not be important for a spheroidal particle due to the axial symmetry. Therefore, Eq.1.21 can be simplified as:

$$\begin{bmatrix} E_\theta^{sca} \\ E_\phi^{sca} \end{bmatrix} = E_0 \frac{e^{ikR}}{R} \boldsymbol{S}(\boldsymbol{n_{inc}}, \boldsymbol{n_{sca}}; \alpha, \beta) \begin{bmatrix} 0 \\ 1 \end{bmatrix}, \tag{2.17}$$

where k is the wave number of the light beam and R is the geometrical length of a given optical path between the examination point and the scatterer.

Once the transformation relationship between incident light and scattered light is established, the focusing and splitter effect in the detector part (see Fig.2.3) must be considered next. In the detector part, the scatterer is located at the focus of the detector lens (Det Lens) while the camera is at the focus of the camera lens (Cam Lens). Thus, the point-source scattered light becomes a plane wave light beam after the Det Lens. Since there is no optical path differences between the two lenses for any valid scattering direction (can go through the Det Lens), the optical path length between the lenses can be neglected during numerical computation.

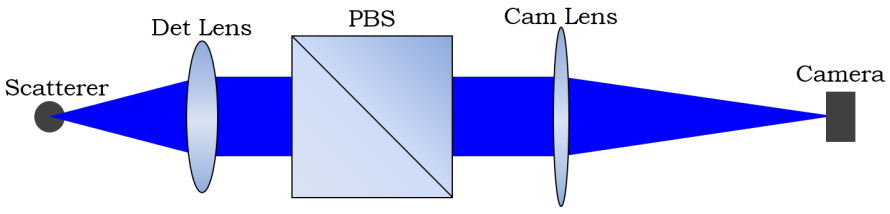

Figure 2.3: Simplified detector part geometry.

Between the two lenses, there is a polarised beam splitter (PBS) that can split the light beam into given polarisation directions. Rather than treat the PBS as a splitter that creates another light beam which still needs some phase correction afterwards, an alternative way is to regard it as two polarisation filters that give different results for each channel directly. The PBS can be rotated about its optical axis to control the polarisation for the two camera channels. The angle of this rotation referred to the x-axis is set to be 45° based on the current set up of SaNTA's design as both channels should have same and significant signals when the particle is isotropic. The

output electric field can be given by:

$$\begin{aligned} \boldsymbol{E}^{+} &= \begin{bmatrix} E_x^{+} \\ E_y^{+} \end{bmatrix} = \frac{1}{2}\begin{bmatrix} 1 & 1 \\ 1 & 1 \end{bmatrix}\begin{bmatrix} E_x \\ E_y \end{bmatrix} \\ \boldsymbol{E}^{-} &= \begin{bmatrix} E_x^{-} \\ E_y^{-} \end{bmatrix} = \frac{1}{2}\begin{bmatrix} 1 & -1 \\ -1 & 1 \end{bmatrix}\begin{bmatrix} E_x \\ E_y \end{bmatrix} \end{aligned} \tag{2.18}$$

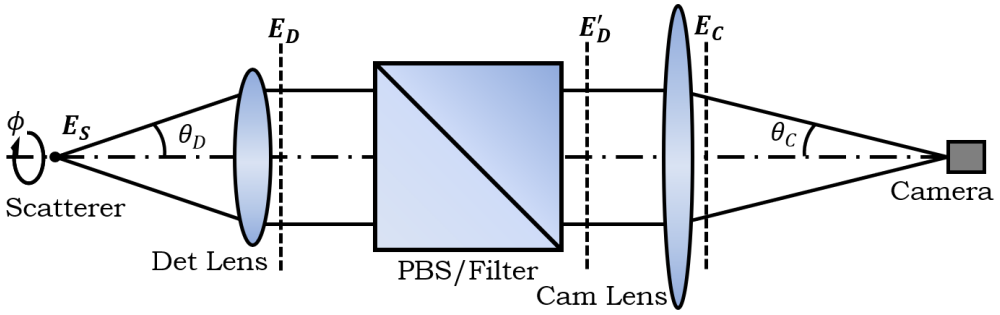

Figure 2.4: Notation for the imaging algorithm

In practice the two lenses have different numerical apertures and focal lengths. The Det Lens has focal length $f_D = 12.7$mm and diameter $\Phi_D = 6.35$mm with clear aperture of 90% which gives the actual diameter about 5.72mm. The Cam Lens has focal length $f_C = 500$mm and diameter $\Phi_C = 25.4$mm with clear aperture of 90% which gives the actual diameter about 22.9mm. The focusing effect of both lenses can be realised by rotating the income light direction by a specific angle which is a function of both the radial position at the lens and the numerical aperture of the lens [38]. For Det Lens and Cam Lens, these angles are denoted by θ_D and θ_C respectively (see Fig.2.4). Both angles can be described by:

$$\begin{aligned} \theta_D &= \arctan\frac{r_D}{f_D} \\ \theta_C &= \arctan\frac{r_C}{f_C} \end{aligned} \tag{2.19}$$

where f_D,f_C are focal lengths of Det Lens and Cam Lens, while r_D and r_C are the radial coordinates of where the light comes in on the lenses. Since the light between two lenses is parallel to the optical axis, r_D should be equal to r_C. Clearly, the angle θ_D denotes the same angle as θ for scattered light, then the angle θ_C can be calculated by:

$$\theta_C = \arctan\left(\frac{f_D}{f_C}\tan\theta\right) \tag{2.20}$$

where $f_D = 12.7$mm, $f_C = 500$mm, and θ can varies from 0 to $\arctan\frac{0.9\Phi_D}{2f_D} = 12.7°$. The light propagation through a lens can be calculated by multiplying several

rotation matrices [39]. Electric vector $\boldsymbol{E_D}$ and $\boldsymbol{E_C}$ can be given by:

$$\begin{aligned} \boldsymbol{E_D} &= \boldsymbol{R^{-1}} \boldsymbol{L_D^{-1}} \boldsymbol{R} \boldsymbol{E_S} \\ \boldsymbol{E_C} &= \boldsymbol{R^{-1}} \boldsymbol{L_C} \boldsymbol{R} \boldsymbol{E_D'} \end{aligned} \tag{2.21}$$

where $\boldsymbol{E_S}$ is the same vector calculated by Eq2.17 but in lab-frame:

$$\boldsymbol{E_S} = \begin{bmatrix} E_x^S \\ E_y^S \\ E_z^S \end{bmatrix} = \begin{bmatrix} \cos\theta\cos\phi & -\sin\phi \\ \cos\theta\sin\phi & \cos\phi \\ -\sin\theta & 0 \end{bmatrix} \begin{bmatrix} E_\theta^S \\ E_\phi^S \end{bmatrix} \tag{2.22}$$

The rotation matrix $\boldsymbol{R}$ and its inverse rotate the light beam into xz-plane and rotate it back after operations so that the light can be simply bent by the lens matrix $\boldsymbol{L}$. These matrices can be given by:

$$\begin{aligned} \boldsymbol{R} &= \begin{bmatrix} \cos\phi & \sin\phi & 0 \\ -\sin\phi & \cos\phi & 0 \\ 0 & 0 & 1 \end{bmatrix} \\ \boldsymbol{L_D} &= \begin{bmatrix} \cos\theta_D & 0 & \sin\theta_D \\ 0 & 1 & 0 \\ -\sin\theta_D & 0 & \cos\theta_D \end{bmatrix} \\ \boldsymbol{L_C} &= \begin{bmatrix} \cos\theta_C & 0 & \sin\theta_C \\ 0 & 1 & 0 \\ -\sin\theta_C & 0 & \cos\theta_C \end{bmatrix} \end{aligned} \tag{2.23}$$

The electric vector detected by the camera is not the whole vector but only the x and y components of it which gives a new electric vector $\boldsymbol{E_C'}$:

$$\boldsymbol{E_C'} = \begin{bmatrix} 1 & & \\ & 1 & \\ & & 0 \end{bmatrix} \boldsymbol{E_C} \tag{2.24}$$

Since the camera is located at the focus of the Cam Lens, the final signal I is actually the integral of the angular intensity distribution $i(\theta_C, \phi)$:

$$I = \iint i(\theta_C, \phi) \mathrm{d}\theta_C \mathrm{d}\phi = \int_0^{2\pi} \mathrm{d}\phi \int_0^{\theta_{C,max}} \mathrm{d}\theta_C \; i(\theta_C, \phi) \tag{2.25}$$

where $\theta_{C,max}$ is the maximum value θ_C can get, which is $\arctan\left(\frac{0.9\Phi_D}{2f_C}\right) = 0.3°$. The angular intensity distribution $i(\theta_C, \phi)$ can be calculated by the dot product of the new electric vector $\boldsymbol{E_C'}$ and its conjugate $\overline{\boldsymbol{E_C'}}$:

$$i(\theta_C, \phi) = \frac{1}{2} \epsilon \overline{\boldsymbol{E_C'}(\theta_C, \phi)} \cdot \boldsymbol{E_C'}(\theta_C, \phi) \tag{2.26}$$

where ϵ is the dielectric permittivity of the air and can be approximated as the vacuum permittivity in normal cases whose value is taken as 1 in the simulation.

Overall, the expression of angular intensity distribution of both plus and minus channels can be given by:

$$\boldsymbol{E}'_{\boldsymbol{C},\pm} = \begin{bmatrix} E_{x,\pm}^{-1} \\ E_{y,\pm}^{-1} \\ E_{z,\pm}^{-1} \end{bmatrix} = \boldsymbol{P}\boldsymbol{R}^{-1}\boldsymbol{L}_{\boldsymbol{C}}\boldsymbol{R}\boldsymbol{F}_{\pm}\boldsymbol{R}^{-1}\boldsymbol{L}_{\boldsymbol{D}}^{-1}\boldsymbol{R}\boldsymbol{T}\begin{bmatrix} E_{\theta}^{sca} \\ E_{\phi}^{sca} \end{bmatrix} \tag{2.27}$$

where $\boldsymbol{P}$ is the projection matrix in Eq.2.24, $\boldsymbol{F}_{\pm}$ is a filter matrix in Eq.2.18 but in 3 dimensions:

$$\boldsymbol{F}_{\pm} = \frac{1}{2}\begin{bmatrix} 1 & \pm 1 & 0 \\ \pm 1 & 1 & 0 \\ 0 & 0 & 0 \end{bmatrix} \tag{2.28}$$

$\boldsymbol{T}$ is the coordinates transform matrix in Eq.2.22.

According to Eq.2.17, Eq.2.27, Eq.2.26 and Eq.2.25, the simulated intensity signal of both channels can be calculated for each given particle orientation which is generated from the Brownian motion generator part. Once a Brownian trajectory is generated, a time sequence of intensities in each channel will be showed, which it is possible to analyse, and which should have the same pattern as the real data measured in experiments.

Chapter 3

Results & Discussion

3.1 Brownian motion simulation

3.1.1 2D Brownian motion of a spheroid and the coupling

According to Eq.1.14, the diffusion coefficients of a spheroid are functions of both volume and aspect ratio. It is easy to show that the volume of the spheroid only changes these coefficients as a scale factor. It does not change the relative values of these coefficients which decides how significant the influence of translation and rotation coupling is. The relationship between diffusion coefficients and aspect ratio of the particle is given by Fig.3.1. The two lines representing two translational diffusion coefficients meets at the point with aspect ratio of 1 which is a sphere. Fig.3.1b shows that the ratio of two translational diffusion coefficients D_a^t/D_b^t will keep increasing but tends to a limit as the aspect ratio increases. The limit of this

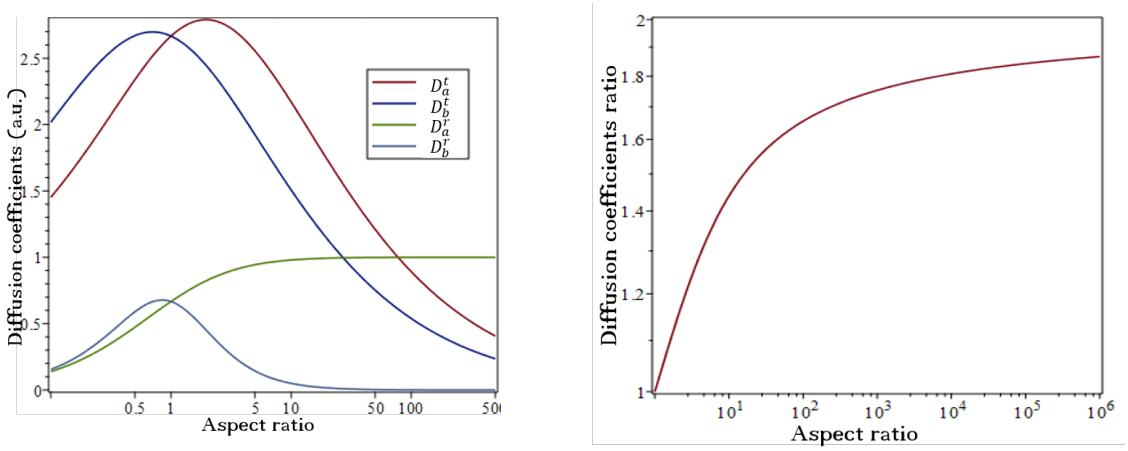

(a) (b)

Figure 3.1: (a) Translational diffusion coefficients along long axis D_a^t and short axis D_b^t, rotational diffusion coefficients about long axis D_a^r and short axis D_b^r plotted against aspect ratio of a spheroidal particle with given volume calculated from Eq.1.14. (b) Ratio of two translational diffusion coefficients D_a^t/D_b^t versus aspect ratio for prolate spheroidal particle (aspect ratio $\rho > 1$) with given volume

ratio is exactly 2 as the aspect ratio goes to infinity, which can be easily proved:

$$\begin{aligned}\frac{D_a^t}{D_b^t} &= \frac{\rho^2(2\beta+\alpha_\parallel)}{2\rho^2\beta+\alpha_\perp} \\ &= \frac{(4\rho^2-2)\beta-2}{(2\rho^2-3)\beta+1} \\ &= 2+\frac{4}{(2\rho^2-3)\beta+1}(\beta-1)\end{aligned} \tag{3.1}$$

where the notation is given by Eq.1.14 and Eq.1.15. Since β is always smaller than 1 but bigger than 0, the term after 2 is smaller than 1 and goes to 0 as the aspect ratio ρ goes to infinity. Q.E.D.

Although the real free spheroidal particle will never have translational diffusion coefficients $D_a^t > 2D_b^t$, it does not change the fact that the translational and rotational motion will be coupling all the time even if it is not a real particle. Therefore, to better visualise the effect of the translation and rotation coupling, the diffusion coefficients along particle axes can be chosen extremely. Fig.3.2 is the Brownian motion trajectory of a non-spherical particle with diffusion coefficients $D_a = 0.99$ and $D_b = 0.01$. Compared with Fig.1.1, the trajectory is sharper at turning points as the particle moves much more along its long axis than the short axis. This can be seen

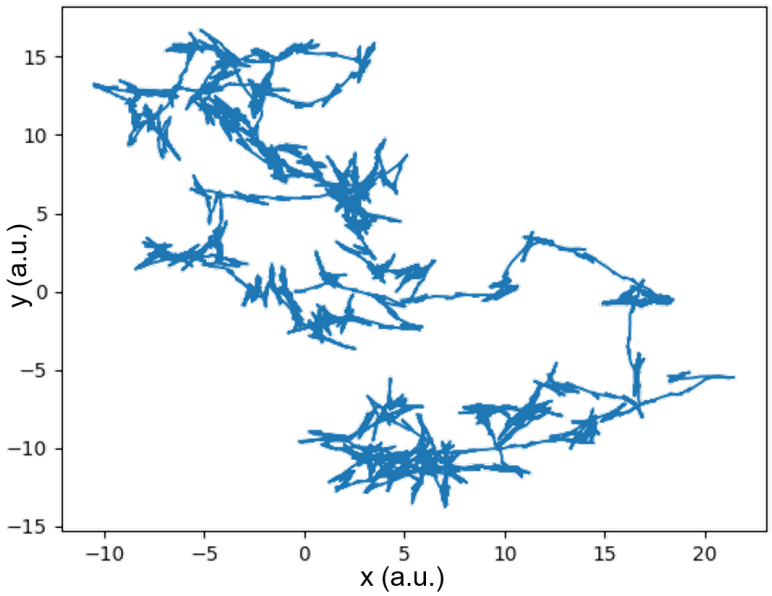

Figure 3.2: Brownian motion trajectory of a particle with diffusion coefficients $D_a = 0.99$, $D_b = 0.01$, and $D_\theta = 1/(2\pi)$ with time step $\delta t = 0.1$ and 1000 points in total

clearer in Fig.3.3 which is the selection of points in the trajectory before the relaxation time of rotation $\tau_\theta = 1/(2D_\theta) = \pi$ along with the particle's orientation (black arrows). All translational movements (blue lines) are almost at the same directions of the particle. Besides, the particle does not rotate much until the time goes to the

relaxation time τ_θ, which is the upper end of the trajectory in this figure. Assuming

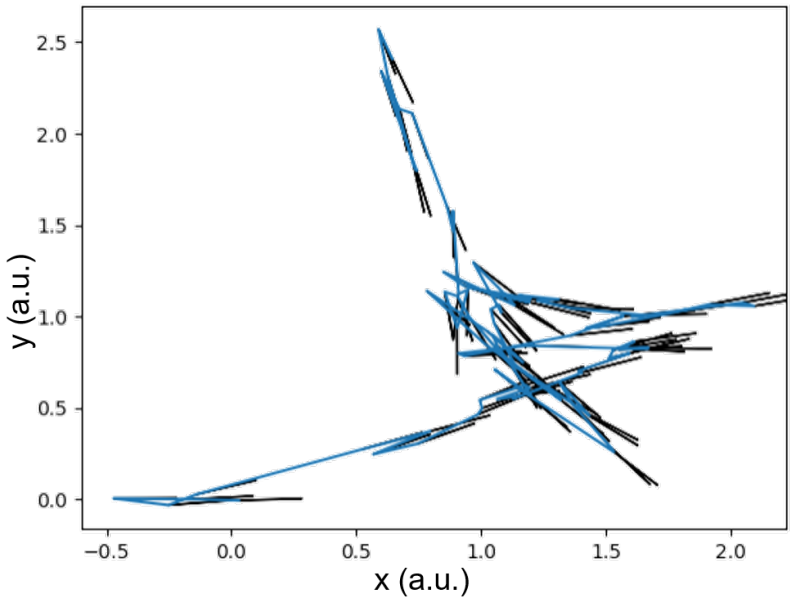

Figure 3.3: Brownian motion trajectory along with particle orientation (black arrows) before the relaxation time of rotation $\tau_\theta = \pi$ (arbitrary unit)

the initial orientation of the particle is along the x-axis, the measured diffusion coefficients along x and y axis as function of time $D_x(t) = \langle x^2 \rangle / 2t$ and $D_y(t) = \langle y^2 \rangle / 2t$ can be plot against time t. The evolution of the two diffusion coefficients is given by Fig.3.4. This figure shows that the measured diffusion coefficients tends to mix up as the time goes beyond the relaxation time rotation τ_θ. They are exactly the values along the the particle axes at the beginning and both end up at the average of them. Therefore, because of the translation and rotation coupling, it would be impossible to tell the difference between a spheroid and a sphere if the measurement time is longer than the relaxation time of rotation τ_θ, which is usually about 20μs for typical nanorod (about 50nm$\times$20nm).

3.1.2 3D rotational Brownian motion

The Brownian motion in 3D space can be hard to show and be expensive to calculate. However, since what really affects the scattering process is its orientation, only the rotational Brownian motion needs to be considered. An intuitive way to show the rotational trajectory is to plot the azimuthal angle and the polar angle as y and x axis, as shown in Fig.3.5. The particle in the simulation is a 48×18nm gold nanorod since it is the particle currently used in the SaNTA testing experiment. By this means, it is possible to visualise the particle orientation just like the displacement in 2D simulation. Both trajectories look alike because they are generated by almost the same mechanism.

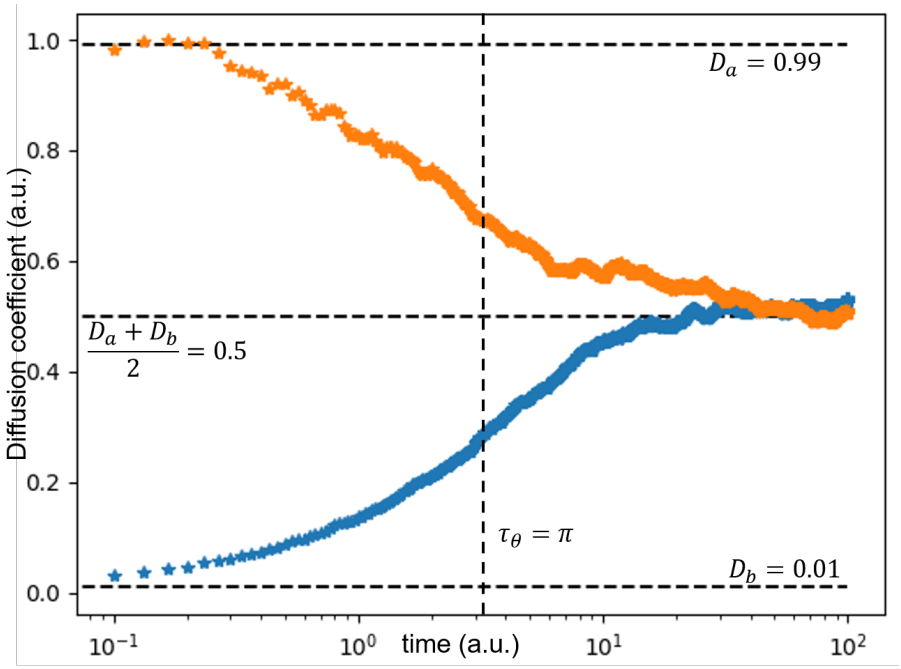

Figure 3.4: Evolution of measured diffusion coefficients D_x (orange) and D_y (blue).

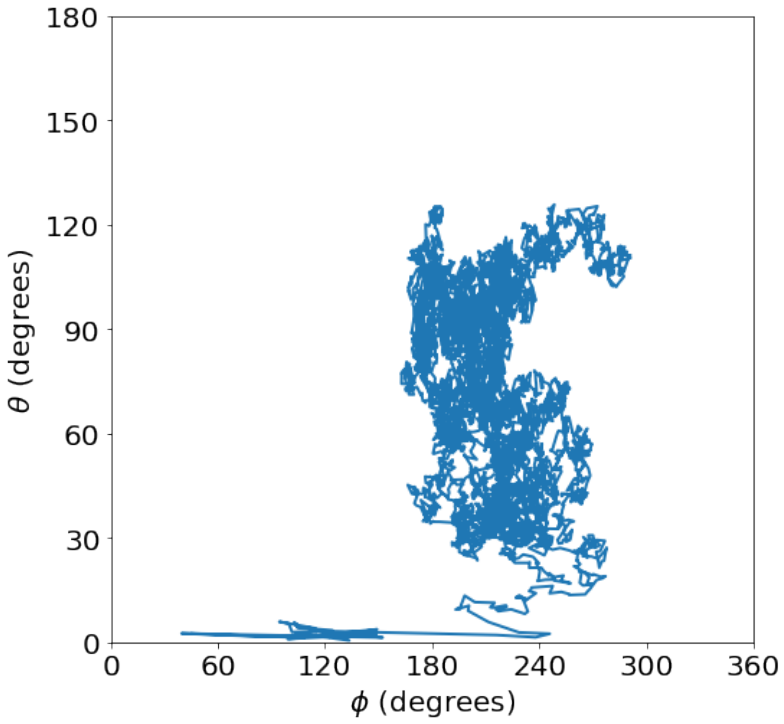

Figure 3.5: Rotational Brownian motion trajectory (orientation coordinate (ϕ, θ)) of a 48nm×18nm gold rod moving in water (viscosity about 0.89mPa·s)

3.2 T-Matrix method study

The verification of the T-Matrix package is done by comparing the Mie scattering result of a spheroid with Asano and Yamamoto's work [37] whose method is solving Maxwell's equations in spheroidal coordinate systems. In this work, the geometry of

the scattering process can be given by Fig.3.6. The scattering results are shown by

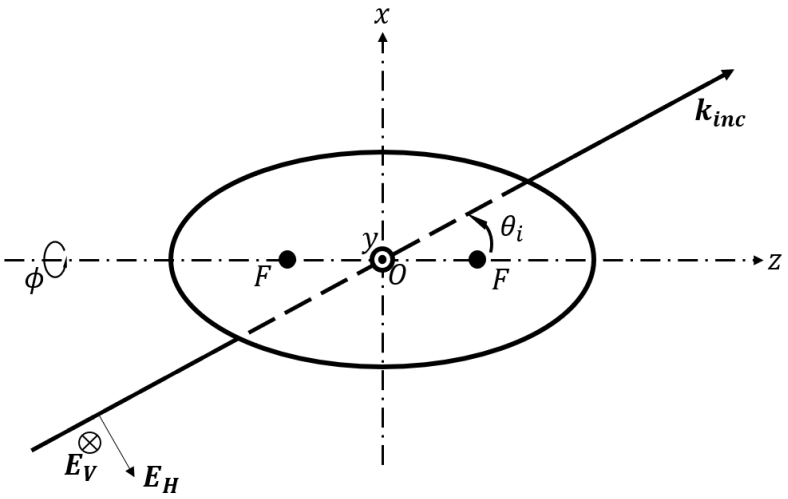

Figure 3.6: Definition of notation to describe Asano and Yamamoto's spheroidal particle scattering work. θ_i is the zenith angle of incident light with polarisation either horizontal (in x-z plane denoted by $\boldsymbol{E_H}$) or vertical (in y-z plane denoted by $\boldsymbol{E_V}$). F denotes the focal points of the spheroid, ϕ denotes the azimuthal angle.

plotting it in a polar diagram against zenith angle θ of scattered light direction with three scattering planes: one parallel to the incident plane ($\phi = 0°$), one inclining from it by 45 degrees ($\phi = 45°$), and one normal to it ($\phi = 90°$); and two polarisations for each plane: parallel and perpendicular to the plane of the z-axis and scattered light. Results for a small prolate spheroid are given in Fig.3.7 and Fig.3.8.

The small prolate spheroid has aspect ratio a/b as 2 and size parameter $c = 1$. The size parameter here is defined by $c = 2\pi nl/\lambda$ where $\lambda = 632.8$nm is the wavelength of incident light and $n = 1.33$ is the refractive index, and $l = 75.7$nm is the semi focal distance OF of the spheroid. Thus, the actual size of this particle is about 175×87.5nm which is quite large for a nanoparticle (compared with the previous 48×18nm gold nanorod). Similar angular distribution polar diagrams have also been plotted for a small oblate spheroid with size parameter $c = 1$ and aspect ratio $a/b = 0.5$ (87.5×175nm) as in Fig.3.9

The particle has two mirror planes when considering the incident light direction - one is the incident plane (plane with incident light and the z-axis) and the other one is the xy-plane ($\theta = 90°$). When the incident angle is $\theta_i = 90°$, the incident light is in the xy-plane and the scattered light in this case should be symmetric about this plane, i.e., the 90°-270° axis in the angular distribution plot as shown in Fig.3.7b and Fig.3.8b. This symmetry will be broken otherwise, e.g., when the incident angle $\theta_i = 45°$ as shown in Fig.3.7a, Fig.3.8a and Fig.3.9. Since the particle is symmetric about the incident plane and only the horizontal and vertical incident light are considered, the scattered light intensity distribution should have mirror symmetry about this plane. Thus, the angular distribution plot for scattering plane $\phi = 90°$ is symmetric about the 0°-180° axis as shown by red lines in Fig.3.7, Fig.3.8

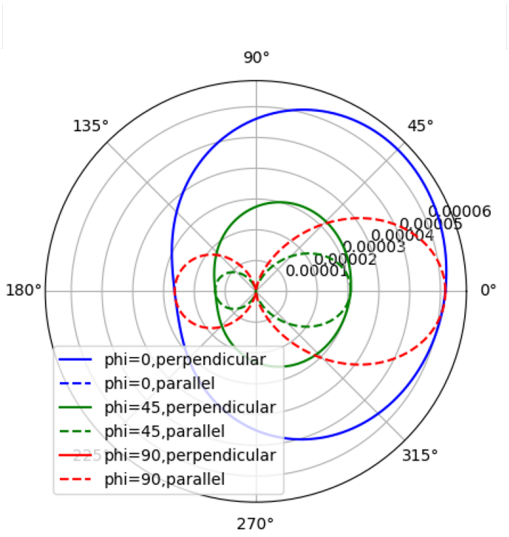

(a) Horizontal incident light with $\theta_i = 45°$

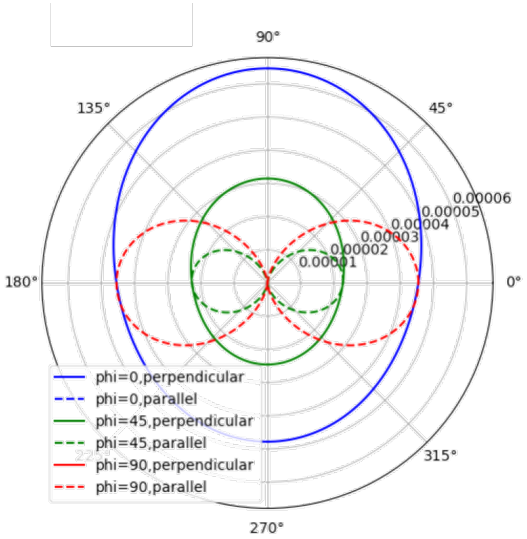

(b) Horizontal incident light with $\theta_i = 90°$

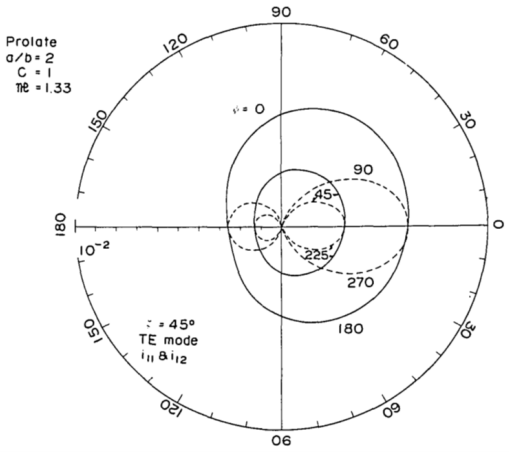

(c) Asano and Yamamoto's result for (a)

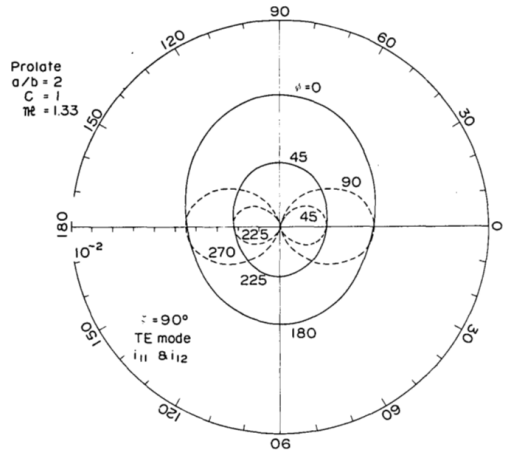

(d) Asano and Yamamoto's result for (b)

Figure 3.7: Angular distribution of intensity with horizontal incident light for a prolate spheroid with aspect ratio $a/b = 2$ and size $c = 1$ (see text). The magnitude is in arbitrary units. The red solid lines in (a) and (b) are vanished because the magnitude is always 0.

and Fig.3.9.

Due to the continuity of electric fields, the scattered electric vector should not be perpendicular to the induced dipole moment which can be calculated by Eq.1.32 for small particles. Therefore, when the scattering plane is the same as the incident plane ($\phi = 0°$), the perpendicular component of scattered light for vertical incident light (blue solid lines in Fig.3.8 and Fig.3.9b) will vanish as well as the parallel component for horizontal incident light (blue dashed lines in Fig.3.7 and Fig.3.9a). For vertical incident light with $\theta_i = 90°$, the perpendicular component of all scattering planes is 0 because the induced dipole moment is at the same direction as the incident electric vector, and is parallel to all scattering planes, which explains why all the solid lines disappeared in Fig.3.8b. Generally, the solid line will disappear when the induced dipole moment is parallel to the scattering plane, whereas the dashed lines disappeared when the induced dipole moment is perpendicular to

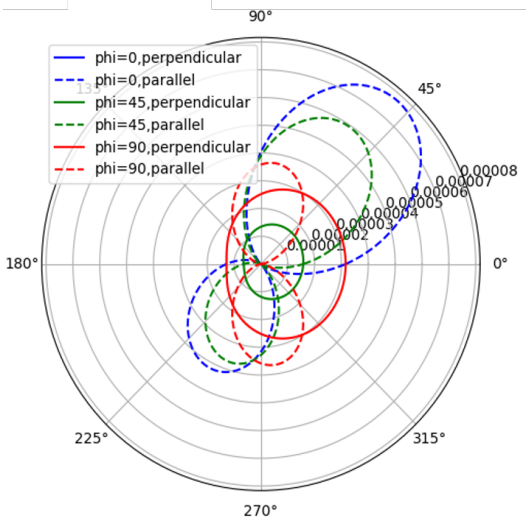

(a) Vertical incident light with $\theta_i = 45°$

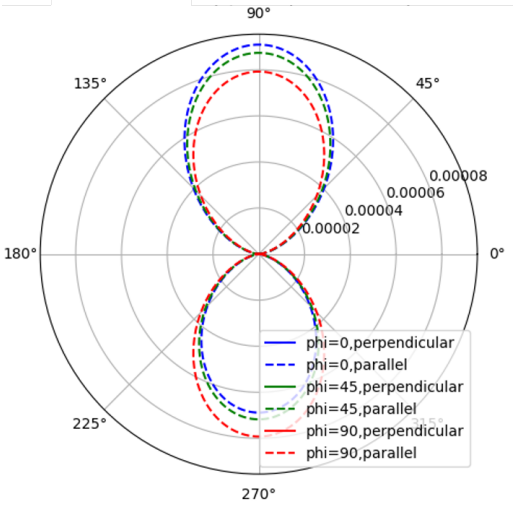

(b) Vertical incident light with $\theta_i = 90°$

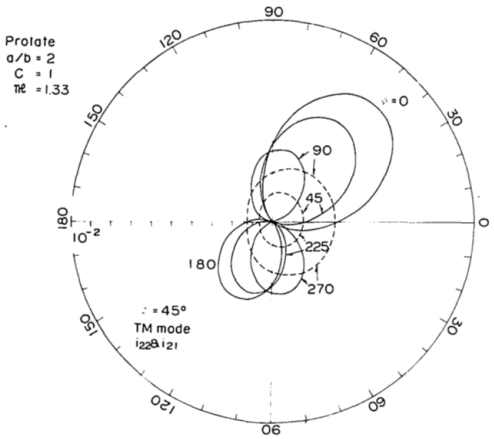

(c) Asano and Yamamoto's result for (a)

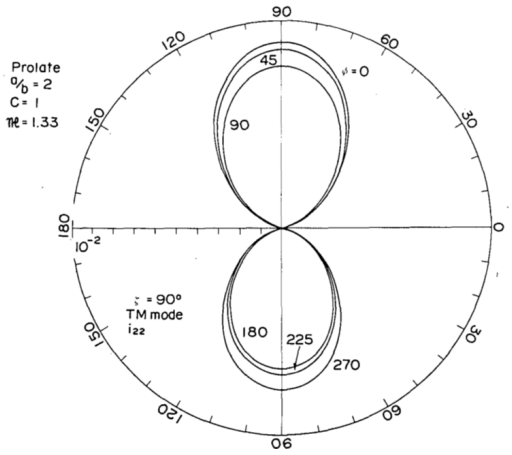

(d) Asano and Yamamoto's result for (b)

Figure 3.8: Angular distribution of intensity with vertical incident light for a prolate spheroid with aspect ratio $a/b = 2$ and size $c = 1$ (see text). The magnitude is in arbitrary units. The blue solid line in (a) and all solid lines in (b) are vanished because the magnitude is always 0.

the scattering plane. There are also some zero points at certain angles where the scattered electric vector is perpendicular to the induced dipole moment.

All these results for the small spheroid look the same as figures in Asano's research. This demonstrates that the T-Matrix method and its code works correctly at least for small particles. However, when the size parameter increases to 5 with the same aspect ratio, i.e., the particle is about 875×437.5nm, the computation time increases extremely and the accuracy decreases (compared with results in Asano's research). This is because the particle is too big, leading to an increase in computational complexity and the time needed to converge. To reach a converged result, more terms for VSWFs and a finer mesh for the surface integral in Eq.1.45 are required.

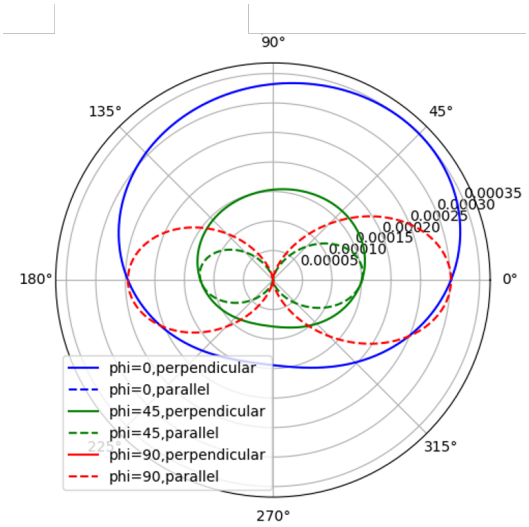

(a) Horizontal incident light with $\theta_i = 45°$

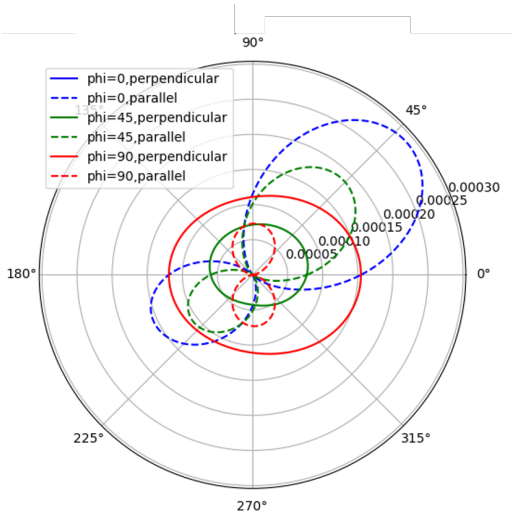

(b) Vertical incident light with $\theta_i = 45°$

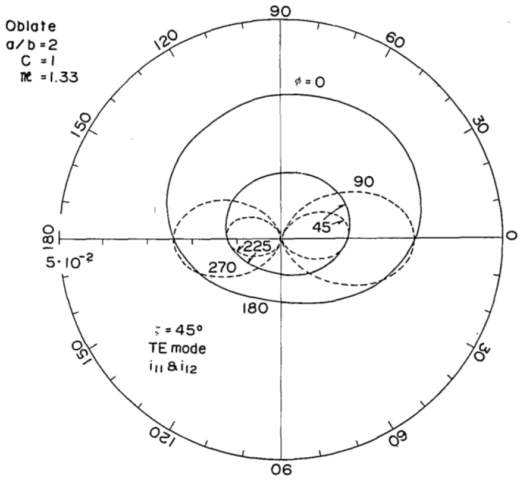

(c) Asano and Yamamoto's result for (a)

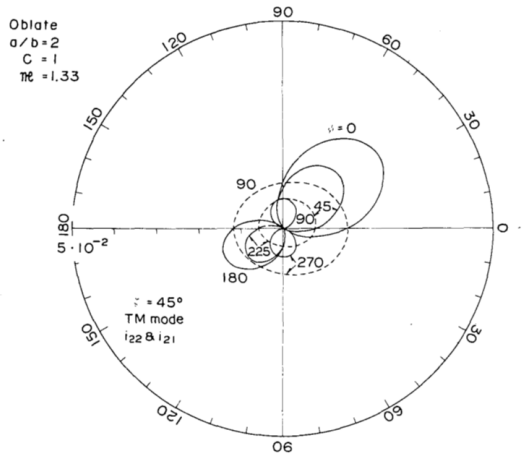

(d) Asano and Yamamoto's result for (b)

Figure 3.9: Angular distribution of intensity for an oblate spheroid with aspect ratio $a/b = 2$ and size $c = 1$ (see text). The magnitude is in arbitrary units. The red solid line in (a) and the blue solid lines in (b) are vanished because the magnitude is always 0.

3.3 Scattering simulation for SaNTA

3.3.1 Intensity map of orientation

Although the intensity signals from a sequence of orientations for the particle is the ultimate object to study, it is still useful to learn how the signals would be for every possible orientation. This can be done by a couple of heatmaps represent the signals as a function of the orientation coordinate (θ, ϕ). When only considering the scattered light along the z-axis, the focusing effect of the lenses and the light propagation can be ignored. The results calculated by the T-Matrix method are shown by Fig.3.10. The result shows that the maximum scattered light intensity happens when the particle lies in the xy-plane ($\theta = 90°$) which agrees with the geometric symmetry. However, the maximum location along the ϕ axis is at 67.5°, which is a little bit against intuition. Although the 48 × 18nm gold nanorod has

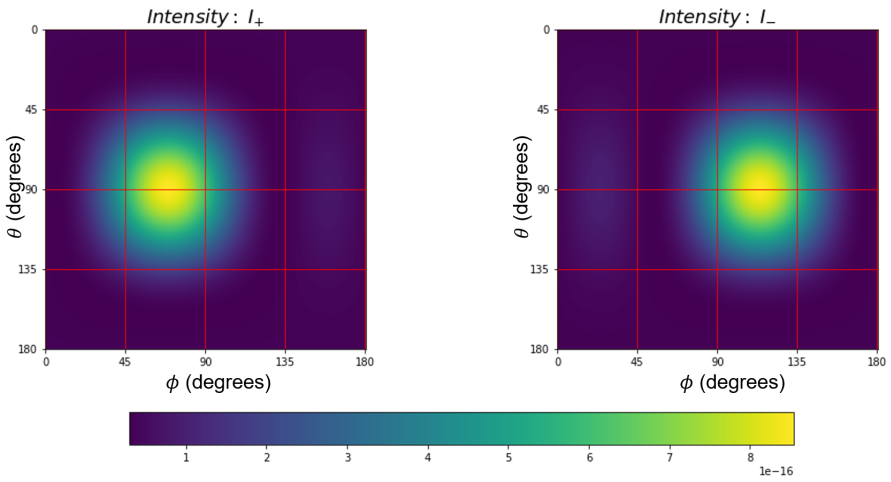

Figure 3.10: Induced dipole moment intensity with polarisation agree with plus and minus channel of SaNTA, i.e., $I_\pm = |E_x \pm E_y|^2$ The magnitude of intensity is in arbitrary units.

size slightly beyond the Rayleigh limit $a/\lambda \ll 0.05$, this result can still be proved by using Rayleigh scattering theory.

Assume the particle is spheroidal and has polarisability α_L along the major axis (long axis) and α_S along the minor axis (short axis), whose expression can be given by Eq.1.34 but it does not really matter. Considering the particle with orientation (θ, ϕ) where θ is the zenith angle and ϕ is the azimuthal angle, the polarisability tensor $\boldsymbol{\alpha}$ can be transformed into the lab-frame (along xyz axes, the matrix is denoted by $\boldsymbol{\alpha}_p$) from the body-frame (the matrix is denoted by $\boldsymbol{\alpha}_l$) by:

$$\begin{aligned}
\boldsymbol{\alpha} &= \begin{bmatrix} \hat{\boldsymbol{l}} & \hat{\boldsymbol{s}}_1 & \hat{\boldsymbol{s}}_2 \end{bmatrix} \begin{pmatrix} \alpha_l & & \\ & \alpha_s & \\ & & \alpha_s \end{pmatrix} \begin{bmatrix} \hat{\boldsymbol{l}} \\ \hat{\boldsymbol{s}}_1 \\ \hat{\boldsymbol{s}}_2 \end{bmatrix} \\
&= \begin{bmatrix} \hat{\boldsymbol{x}} & \hat{\boldsymbol{y}} & \hat{\boldsymbol{z}} \end{bmatrix} \boldsymbol{R}\boldsymbol{\alpha}_{\boldsymbol{p}}\boldsymbol{R}^{-1} \begin{bmatrix} \hat{\boldsymbol{x}} \\ \hat{\boldsymbol{y}} \\ \hat{\boldsymbol{z}} \end{bmatrix} \\
&= \begin{bmatrix} \hat{\boldsymbol{x}} & \hat{\boldsymbol{y}} & \hat{\boldsymbol{z}} \end{bmatrix} \boldsymbol{\alpha}_{\boldsymbol{l}} \begin{bmatrix} \hat{\boldsymbol{x}} \\ \hat{\boldsymbol{y}} \\ \hat{\boldsymbol{z}} \end{bmatrix}
\end{aligned} \tag{3.2}$$

where $\hat{\boldsymbol{x}}, \hat{\boldsymbol{y}}, \hat{\boldsymbol{z}}$ are the basis vectors of the lab-frame and $\hat{\boldsymbol{l}}, \hat{\boldsymbol{s}}_1, \hat{\boldsymbol{s}}_2$ are the basis vectors of the body-frame (long axis and two short axis). $\boldsymbol{R}$ is the rotation matrix given by:

$$\boldsymbol{R} = \begin{bmatrix} \sin\theta\cos\phi & \cos\theta\cos\phi & -\sin\phi \\ \sin\theta\sin\phi & \cos\theta\sin\phi & \cos\phi \\ \cos\theta & -\sin\theta & 0 \end{bmatrix} \tag{3.3}$$

and

$$\begin{bmatrix} \hat{\boldsymbol{x}} \\ \hat{\boldsymbol{y}} \\ \hat{\boldsymbol{z}} \end{bmatrix} = \boldsymbol{R} \begin{bmatrix} \hat{\boldsymbol{l}} \\ \hat{\boldsymbol{s}}_1 \\ \hat{\boldsymbol{s}}_2 \end{bmatrix} \tag{3.4}$$

Then, the induced dipole moment can be given by:

$$\boldsymbol{p} \propto \boldsymbol{\alpha_p} \boldsymbol{E}^{inc} \propto \boldsymbol{R} \boldsymbol{\alpha_l} \boldsymbol{R}^{-1} \boldsymbol{E}^{inc} \tag{3.5}$$

where $\boldsymbol{E}^{inc}$ is the incident electric vector in the lab-frame, and in this problem it only has a y-component E_0. The dipole moment in the plus and minus channels $\boldsymbol{p}_\pm$ can be given by

$$\boldsymbol{p}_\pm = \frac{1}{2} \begin{bmatrix} 1 & \pm 1 & \\ \pm 1 & 1 & \\ & & 0 \end{bmatrix} \boldsymbol{p} \tag{3.6}$$

Thus,

$$\begin{aligned} \boldsymbol{p}_\pm &\propto \frac{1}{2} \begin{bmatrix} 1 & \pm 1 & \\ \pm 1 & 1 & \\ & & 0 \end{bmatrix} \boldsymbol{R} \boldsymbol{\alpha_l} \boldsymbol{R}^{-1} \begin{bmatrix} 0 \\ E_0 \\ 0 \end{bmatrix} \\ &\propto \frac{E_0}{2} \begin{bmatrix} (\alpha_l \sin^2\theta + \alpha_s \cos^2\theta) \sin\phi (+\cos\phi \pm \sin\phi) + \alpha_s \cos\phi (\pm\cos\phi - \sin\phi) \\ (\alpha_l \sin^2\theta + \alpha_s \cos^2\theta) \sin\phi (\pm\cos\phi + \sin\phi) + \alpha_s \cos\phi (+\cos\phi \mp \sin\phi) \\ 0 \end{bmatrix} \\ &\propto \frac{E_0}{2} \begin{bmatrix} +(\alpha_l - \alpha_s) \sin^2\theta \sin\phi (\cos\phi \pm \sin\phi) \pm \alpha_s \\ \pm(\alpha_l - \alpha_s) \sin^2\theta \sin\phi (\cos\phi \pm \sin\phi) + \alpha_s \\ 0 \end{bmatrix} \end{aligned} \tag{3.7}$$

It is obvious that the p_x and p_y components always have the same absolute value $p_\pm$ for both plus and minus channels. Since the intensity satisfies

$$I_\pm \propto (p_{x,\pm}^2 + p_{y,\pm}^2) = 2p_\pm^2, \tag{3.8}$$

the maximum location of intensity can be found by the zero point of its first derivative of angle θ or ϕ:

$$\frac{\partial I_\pm(\theta,\phi)}{\partial(\theta,\phi)} = 4p_\pm(\theta,\phi) \frac{\partial p_\pm(\theta,\phi)}{\partial(\theta,\phi)} \tag{3.9}$$

Clearly, the solution of equation $p(\theta,\phi) = 0$ does not always exist and it should not be the maximum location of intensity as it gives a value of 0 for the non-negative

intensity. Therefore, the maximum location should satisfy

$$\begin{aligned} \frac{\partial p_{\pm}(\theta,\phi)}{\partial \theta} &= |(\alpha_l - \alpha_s)\sin 2\theta \sin\phi(\cos\phi \pm \sin\phi)| \; = 0, \quad \forall\phi \in [0, 360°) \\ \frac{\partial p_{\pm}(\theta,\phi)}{\partial \phi} &= |\sqrt{2}(\alpha_l - \alpha_s)\sin^2\theta\cos(2\phi \mp 45°)| \; = 0, \quad \forall\theta \in [0, 180°) \end{aligned} \tag{3.10}$$

which gives $\theta = 90°$, $\phi = 67.5°$ for plus channel and $\theta = 90°, \phi = 112.5°$ for minus channel. The heatmap of intensity calculated this way is shown by Fig.3.11.

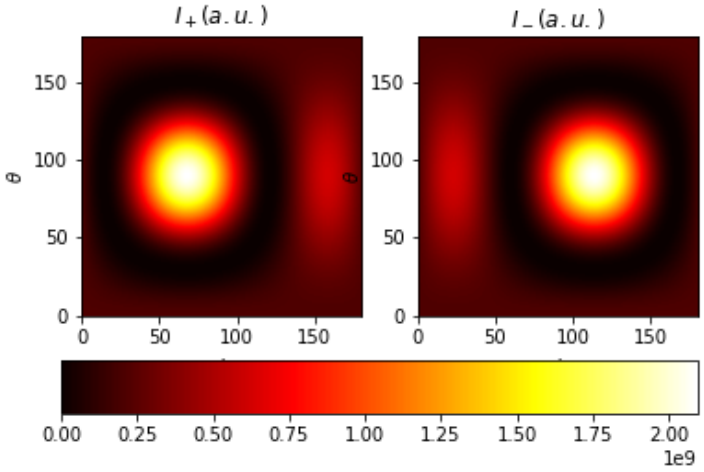

Figure 3.11: Induced dipole moment intensity with polarisation in agreement with plus and minus channels of SaNTA as calculated by Rayleigh theory.

3.3.2 Time dependent signals analysis

The time dependent signal sequence is obtained by calculating the scattering process for a rotational Brownian motion trajectory for a given particle, time step, and total number of steps. In this part, the particle is set to be the 48×18nm gold nanorod in water (viscosity $\mu = 0.89$mPa•s) which is approximated as a spheroid for simplicity. The translational diffusion coefficients of this particle are $D_a = 20.497\mu m^2/s$ and $D_a = 16.997\mu m^2/s$. The rotational diffusion coefficient of the major axis is $D_\theta = 46797(\text{rad})^2/\text{s}$, which gives the relaxation time of rotation $\tau_\theta = 10.684\mu s$. The rotational diffusion coefficients of the minor axis will not influence the behaviour of Brownian motion because of the symmetry and thus are ignored. The temperature of simulation is at room temperature $T = 300K$.

Apart from the direct result of the scattered light intensity of the sequence of rotations, another technique that considers the actual mechanism of signal detection is adapted. Since the frame rate of the camera is rather slow, the signal it detects is not the intensity at a particular time but an integration of all intensity between two frames. Therefore, the actual signal is the integration over subsequences, with certain length, of the high time resolution sequence (the direct result) which gives

a lower time resolution sequence.

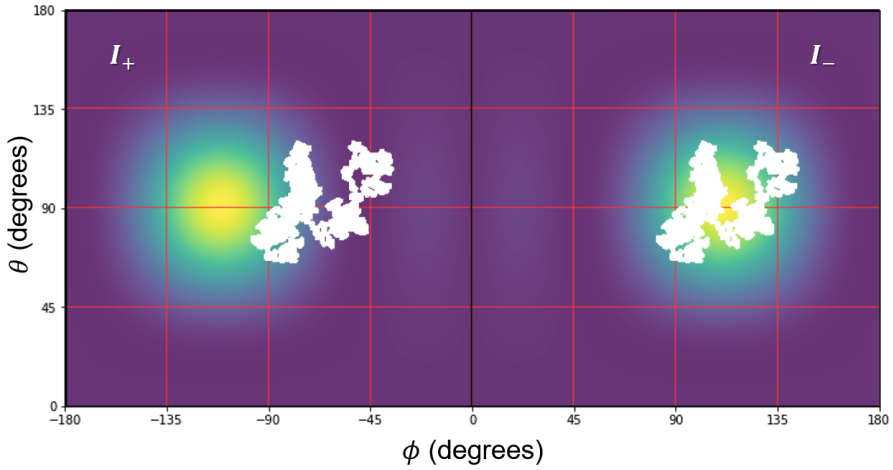

Figure 3.12: Rotational Brownian motion trajectory (white line) compared with the intensity map over orientation (background). The left part is for the plus channel while the right part is for the minus channel. The trajectory on the right is a copy the trajectory on the left in order to compare with the intensity map.

When the integrated time resolution is much higher than the relaxation time or rotation , i.e., integration time $\ll \tau_\theta$ (about $10\mu s$), the signal should be correlated, and the orientation distribution should be localised in a certain time scale. Fig.3.12 shows a rotational Brownian motion trajectory (white line) with time step 1ns and 10000 total steps (total $10\mu s$ for measurement) compared with the intensity map over orientation in both channels mentioned in Fig.3.11 (the background). The

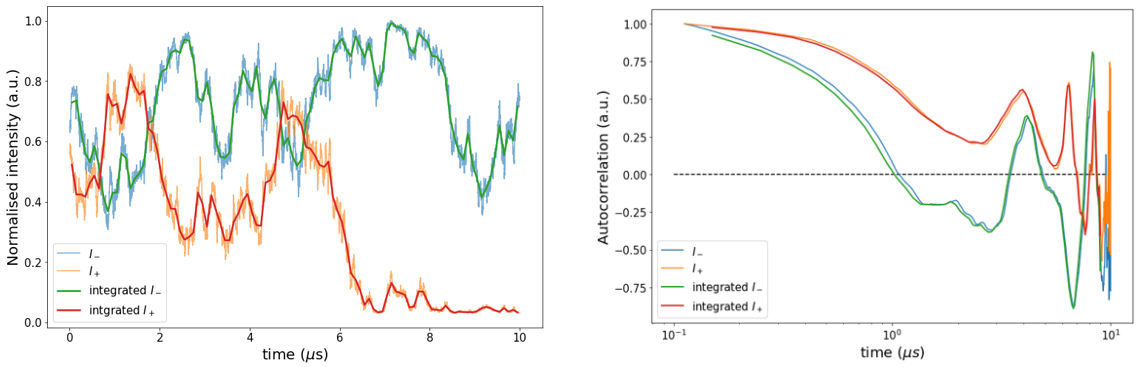

(a) (b)

Figure 3.13: (a) Direct (shallow orange and blue) and integrated (red and green) signals of plus and minus channels. (b) Autocorrelation function of corresponding signals.

corresponding intensity signal sequence and integrated signal is shown by Fig.3.13a. The integration is over subsequences with a length of 100 points, i.e., the time step for the integrated intensity signal is $0.1\mu s$. Both direct signals and integrated signals are normalised by the maximum value for both channels. Also shown in Fig.3.13b is the autocorrelation function of the four signals. In the region far before the relaxation time of rotation ($10\mu s$), all four signals are highly self-correlated. When

the time comes to the relaxation time, the ACF start fluctuating around 0 which indicates the signal is no longer correlated.

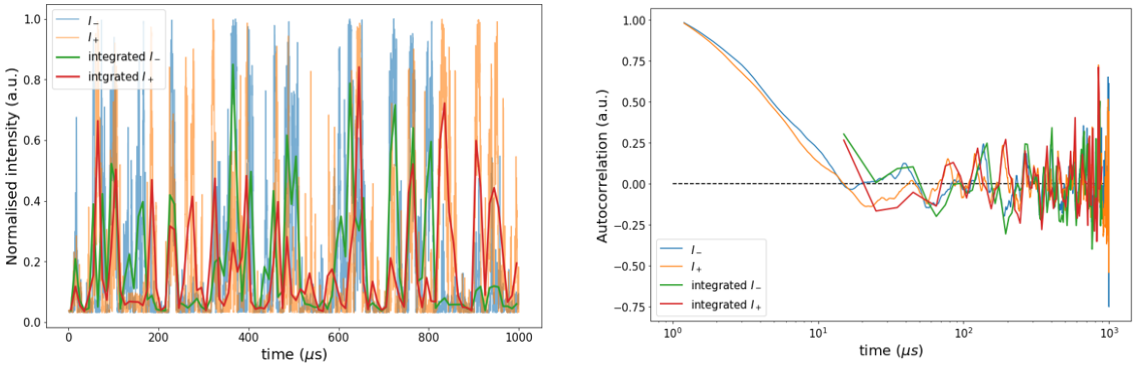

(a) (b)

Figure 3.14: (a) Simulation (shallow orange and blue) and integrated (red and green) signals of plus and minus channels. (b) Autocorrelation function of corresponding signals. The orange and blue lines are the signals before the integration whereas the red and green lines are the signals after the integration.

A similar study has also been applied on a trajectory Fig.3.14 with time step of $0.1\mu s$ (simulation time step) and total 10000 time-steps while the integration step is still 100 point which gives a time step after integration of $10\mu s$. The reason for choosing this trajectory is that the time step of direct signals is much smaller than the relaxation time of rotation while the integrated time step is near it. If the integration is effective for giving additional correlation of signals compare with direct measurement (raw data of simulation before integration), the ACF of the integrated signals should still have a positive and stable value rather than fluctuating around zero at the relaxation time of rotation, i.e., about 10μs. Fig.3.14b shows that there is no significant difference between integration method and direct measurement around the relaxation time of rotation.

3.3.3 Size anisotropy analysis

When studying the effect of size anisotropy of the particle, a pattern has been found for the scatter plot of plus channel intensity signal (I_+) against minus channel signal (I_-). It seems that when the equal volume radius is assumed, i.e., the volume of the particle is a constant, the collection of the normalised intensity coordinate (I_+, I_-) tends to change from a single point at the upper right corner (1,1) for a sphere, to an isosceles right triangle filling the whole lower left corner (a triangle with vertices (0,0),(0,1),(1,0)) as the aspect ration tends to large values and the particle becomes more rod-like, as shown in Fig.3.15. Theoretically, the shape of the intensity scatter plot should be symmetric about the line $I_+ = I_-$, thus the maximum value of $(I_+ + I_-)/2$ should monotonically decrease from 1 to the limit of 1/2 as the aspect ratio varies from 1 to infinity. Let $I_m = \max(I_+ + I_- - 1)$ be the value describing

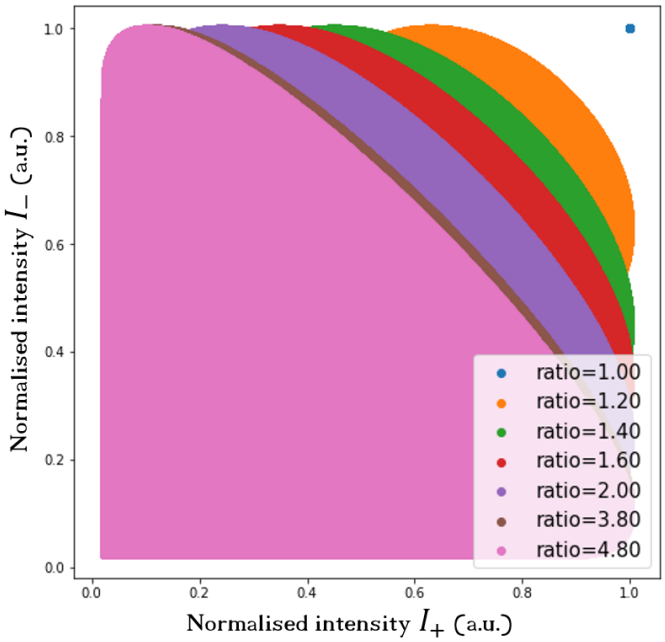

Figure 3.15: Collection of normalised intensity coordinate (I_+, I_-) for different aspect ratio with same volume. The equal volume radius is 0.01 wavelength which is about 5.3nm.

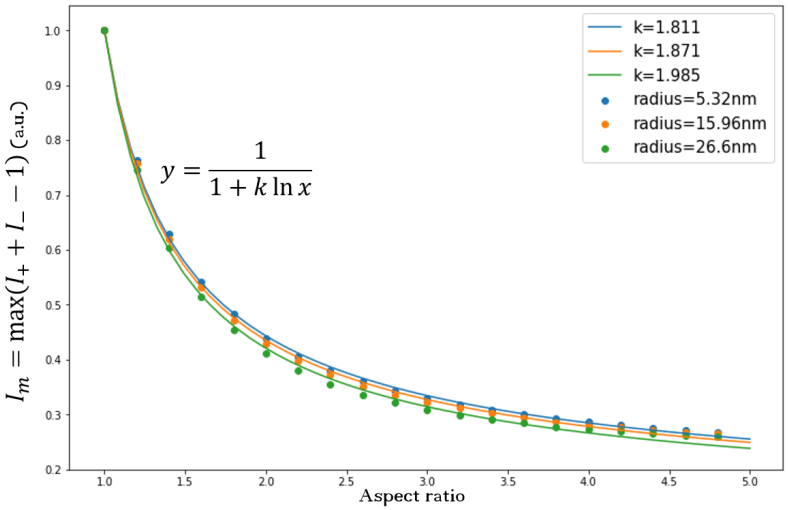

Figure 3.16: Relationship between the value I_m and aspect ratio for particles with different equal volume radius. This relationship can be well fitted by function $y = \frac{1}{1+k \ln x}$.

this relationship, then the aspect ratio - I_m plot can be shown as Fig.3.16 for particles with different equal volume radius. Although the exact expression is unclear, the relationship can be fitted approximately by the function $y = \frac{1}{1+k \ln x}$, with parameter k related to the volume of the particle as shown in the figure.

3.3.4 Discussion

As indicated above, there are two ways to extract information concerning the size anisotropy from a sequence of intensities.

One is calculating the ACF of the two channels and fitting it with the function $ACF = [\exp(-kt)]^2$ where k is a coefficient related to the translational and rotational diffusion coefficients, the scattering angle, and the wavelength of incident light. This method faces two major problems. The first problem is that the exact expression of the ACF for $+45°$ and $-45°$ polarisation is still unclear. It can be converted into combinations of ACF of the polarised scattered light signals and the depolarised scattered light signals and the cross-correlation between them indeed, but the expression could be massive and inoperable. This problem can be solved by replacing the $\pm 45°$ channels by $0°$ and $90°$ polarisation channels that agree with the geometry of the polarised and the depolarised light scattering. This change is already in progress to improve SaNTA's experimental geometry. Another problem is that the ability to observe and calculate the ACF requires a high frame rate camera that gives time resolution much higher than the relaxation time of the particle, see Fig.3.17. Such cameras are expensive and not readily available. Besides, the ACF

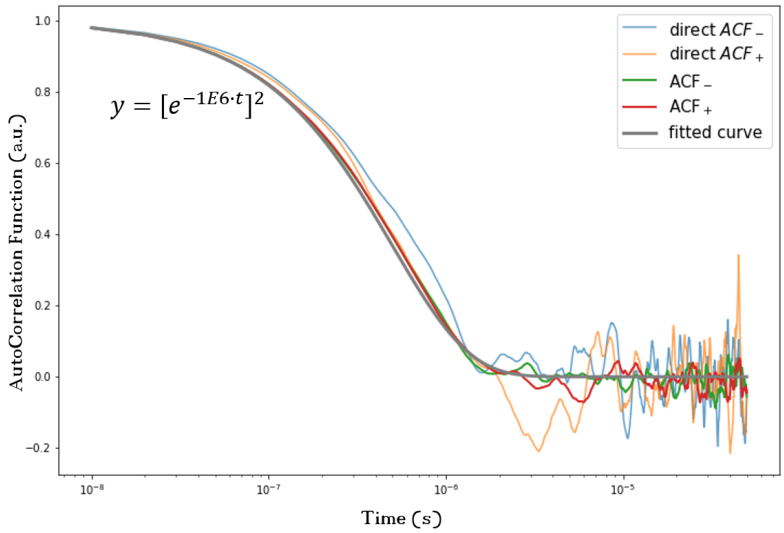

Figure 3.17: The orange and blue lines are autocorrelation functions of a single trajectory. The red and green lines are the average autocorrelation functions of ten trajectories which is equivalent to ten subsequences of a long trajectory. All trajectories have time-steps of 10ns while the relaxation time of rotation is about 10μs. The average ACF has lesser noise than ACF of a single trajectory and can be fitted by function $y = [e^{-10^6 t}]^2$.

of a single nanoparticle tracking signal is sensitive and unstable. It is possible to stabilise the ACF for a single particle by slicing the signal sequence into several pieces and taking an average over all ACFs of a single piece, provided the time dependent signal sequence is long enough. This requires that the particles should stay in the incident light sheet as long as possible and rotate as slowly as possible, which can be achieved by increasing the viscosity of the liquid, e.g. replace it with glycerol (viscosity 0.934Pa•s). It is also possible to control the viscosity over a wide range if a mixture of glycerol and water is used. As the relaxation time of rotation is proportional to the viscosity and the volume of the particle, if the viscosity in-

creases by a factor of 1000, i.e., replacing water by glycerol, the relaxation time will also increases by a factor of 1000. For the 48 × 18nm gold nanorod, the relaxation time can increase from about 10μs to 10ms which is comparable with the frame rate of current cameras. Therefore, increasing the viscosity is a possible way to get a relaxation time large enough compare with the camera's frame rate if the particle is larger than this. Fig.3.18 shows the ACF of a particle with aspect ratio of 3 and equal volume radius of 21.28nm in glycerol (relaxation time about 50ms). This indicates that increasing of viscosity can slow down the rotation speed to a suitable range for experiments.

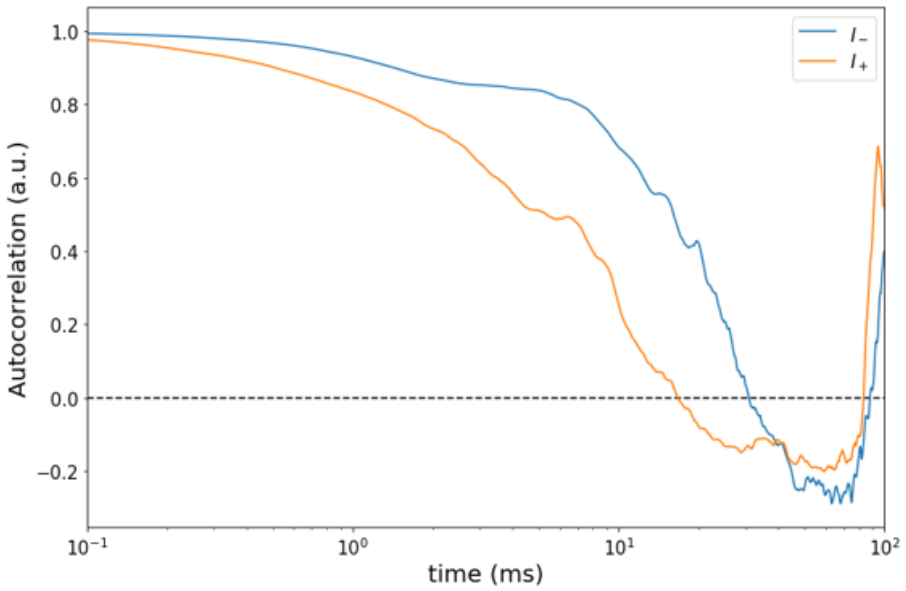

Figure 3.18: ACF for a particle with aspect ratio of 3 and the equal volume radius of 21.28nm in a high viscosity environment (glycerol).

Another method is to calculate the maximum value of $I_+ + I_- - 1$, which is decreasing from 1 to 0 as the aspect ratio varies from 1 to infinity. The function $y = \frac{1}{1+k \ln \rho}$ seems to be able to describe this relationship approximately where k is a parameter related with particle's volume while ρ is the aspect ratio of the particle. The benefit of this method is that it does not require a very high time resolution for the camera. But the general validity of this function is still untested and the physical principle of it is also unclear. Unlike the ACF method, it actually needs a relatively low time resolution to get enough samples for all orientations. When the relaxation time increases with viscosity to the level of camera's frame rate, it seems that it is hard to have enough samples in the intensity scatter plot to find an accurate maximum value of $I_+ + I_- - 1$ as the volume of the particle increases as shown in Fig.3.19. To have more results available, the translational motion of the particle should be as slow as possible, which can also be satisfied by increasing the viscosity. However, the viscosity cannot be too high in this method as it will slow the rotational motion and decrease the efficiency of sampling. Thus, the balance

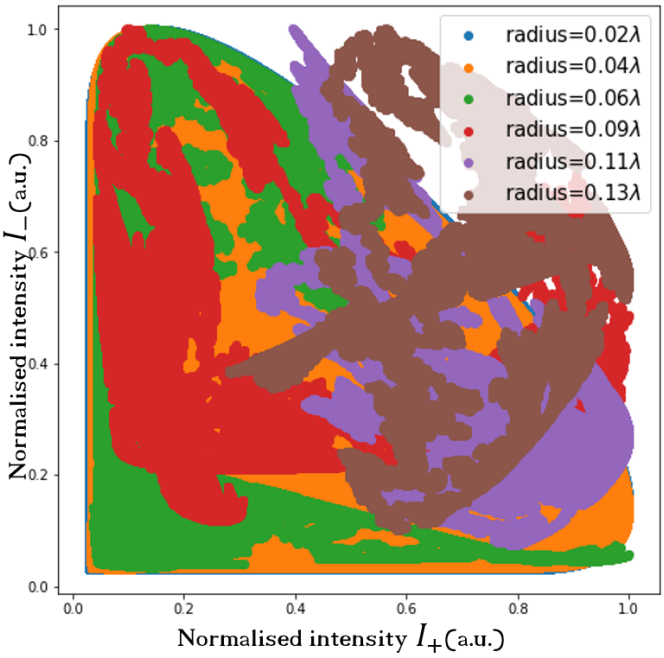

Figure 3.19: Intensity scatter plot for particles with different volume while the aspect ratio is held at 3 in glycerol. The equal volume radius of these particles varies from 0.02λ to 0.13λ where $\lambda = 532$nm is the wavelength of incident light. All trajectories involved have a total 10000 sample points with 1μs simulation time-step. As the volume increases and so as the relaxation time, the shape of the scatter plot starts to be fragmented. Since it does not satisfy the symmetry required (symmetric about straight line $I_+ = I_-$), this problem appears to be due to a lack of sampling when the trajectory is coupling with its initial orientation.

point of the viscosity needs to be carefully chosen and still requires further studies.

Therefore, in either way for extracting the size anisotropic information, increasing of viscosity by a suitable amount can give a wide possible parameter space to achieve the goal.

Experiments are planned using the mixtures of water and glycerol to test the validity of these methods in real life, but these have been prevented by the influence of COVID-19 pandemic unfortunately. So there is no direct experimental comparison possible currently.

Chapter 4

Conclusion

4.1 Conclusion

Currently, the validity and limitation of the T-Matrix method-based model has been proved by comparing with other literatures. An intuitive representation of the relationship between particle orientation and scattered light intensity signals for the $+45°$ and $-45°$ polarisation channels has been established. Analysis and simulations give two potential methods to achieve the goal of extracting size anisotropic information from the single particle tracking technique. One is calculating the autocorrelation function of intensity signals. To get better performances and understandable data, a technique such as measuring the polarised and depolarised light scattering instead of $\pm 45°$ polarisation and slicing the long signal sequence into short sequences and taking an average over ACFs for short sequences can be adopted. The other method is to take enough samples for the intensity channel scatter plot and finding I_m, the maximum value of $I_+ + I_- - 1$. Both methods could benefit from increasing the viscosity of the solution to a proper range, which can slow both the rotational motion that gives relatively higher time resolution for camera and the translational motion that can hold the particle longer in the incident light sheet to obtain more intensity signals. There are still some mysteries unsolved e.g., the physical principle of the expression for the relationship between I_m and the aspect ratio, why it gets harder to fully sample for the intensity scatter plot as the volume gets larger, how would ACF method perform when the intensity signals come from the polarised and the depolarised channels, etc. These questions should be able to be fully explained in the future.

4.2 Future Works

The first work that can be done in the future is to explore the average ACF for the polarised and depolarised light signals, since SaNTA is being updated to replace the original $\pm 45°$ polarisation channels by $0°$ and $90°$ polarisation channels which

is looking at the polarised and the depolarised scattered light respectively. Thus, the ACF of signals from these channels would be the most potential way to achieve the goal. Besides, the exact expressions of average ACF for the polarised and the depolarised signals are already given by Eq.1.55 and Eq.1.56. Therefore, the plan for this work can be divided into four steps:

1 Adjust the model to get intensity signals for the polarised and the depolarised channels.

2 Slice the signal into pieces and calculating average ACF.

3 Use the equations above and a least square algorithm to fit the average ACF.

4 Solve for the aspect ratio and size parameter from diffusion coefficients.

The second work is to further the intensity scatter plot shape study, which aims to solve two problems. One is the physical principles of the approximate relation $I_m = \frac{1}{1+k\ln\rho}$ and its exact expression. The other is to further explore the relationship between the scatter plot shape and the volume of the particle in a wider range.

Since experimental result for single particle tracking on SaNTA is held up due to the influence of COVID-19, the simulation result cannot be compared with it. But in the future, as lab work is restored, the comparison between simulations and experiments can be proceed, which will hopefully give exciting results.

Bibliography

[1] F. Richard, "The Brownian movement," in *The Feyman Lecture on Physics, Volume I*, ch. 41, New York: Basic books, new millennium ed., 1964.

[2] S. F. E. M. Doi, *The Theory of Polymer Dynamics*. International Series of Monographs on Physics, Oxford University Press, USA, 1988.

[3] A. Einstein and R. Fürth, *Investagation on the Theory of Brownian Movement*. New York: Dover Publications, 1956.

[4] N. Wiener, *Norbert Wiener: Collected Works, Volume 1 Mathematical Philosophy and Foundations; Potential Theory; Brownian Movement, Wiener Integrals, Ergodic and Chaos Theories, Turbulence and Statistical Mechanics*. Cambridge, MA: MIT Press, 1976.

[5] T. G. van de Ven, "Brownian motion of non-interacting colloidal particles," in *Colloidal Hydrodynamics* (T. G. van de Ven, ed.), ch. 2, p. 75, London: Academic Press, 4 ed., 1989.

[6] F. Perrin, E. Stahel, H. Ketelaar, J. Dufay, J. Gauzit, S. Gawronski, S. Gawronski, M. Meunier, J. Andriot, A. Piekara, and Others, "Brownian motion of an ellipsoid-I. Dielectric dispersion for ellipsoidal molecules. Mouvement brownien d'un ellipsoide-I. Dispersion diélectrique pour des molécules ellipsoidales," *Journal de Physique et le Radium*, vol. 5, no. 10, p. 497, 1934.

[7] H. Brenner, "Rheology of a dilute suspension of axisymmetric Brownian particles," *International Journal of Multiphase Flow*, vol. 1, no. 2, pp. 195–341, 1974.

[8] S. Prager, "Interaction of Rotational and Translational Diffusion," *Journal of Chemical Physics*, vol. 23, no. 12, pp. 2404–2407, 1955.

[9] M. Kerker, "CHAPTER 1 - Introduction," in *The Scattering of Light and Other Electromagnetic Radiation* (M. KERKER, ed.), vol. 16 of *Physical Chemistry: A Series of Monographs*, pp. 1–7, Academic Press, 1969.

[10] M. I. Mishchenko, J. W. Hovenier, and L. D. Travis, "Introduction," in *Light Scattering by nonspherical Particles*, ch. 1, pp. 1–28, San Diego: Academic Press, 2000.

[11] L. Tsang, J. A. Kong, and R. T. Shin, "Radiative transfer theory - extinction matrix, emission vector, and scattering phase matrices," in *Theory of Microwave Remote Sensing*, ch. 3, pp. 119–218, New York: Wiley-Interscience, 1985.

[12] H. van de Hulst, "Polarized light and symmetry relations," in *Light Scattering by small particles*, ch. 5, pp. 40–62, New York: Dover Publications, Inc., 1957.

[13] M. Kerker, "Scattering by a sphere," in *The Scattering of Light and Other Electromagnetic Radiation*, ch. 3, pp. 17–96, New York: Academic Press, Inc, 1969.

[14] J. A. Stratton, "Radiation," in *Electromagnetic Theory*, ch. VIII, pp. 424–481, John Wiley & Sons, Ltd, 2015.

[15] M. Kerker, "Anisotropy," in *The Scattering of Light and Other Electromagnetic Radiation*, ch. 10, pp. 574–619, New York: Academic Press, Inc, 1969.

[16] M. I. Mishchenko, J. W. Hovernier, and L. D. Travis, "T-Matrix Method and Its Applications," in *Light Scattering by nonspherical Particles Theory, Measurements, and Applications*, ch. 6, pp. 147–173, 2000.

[17] M. Abramowitz and I. A. Stegun, *Handbook of mathematical Functions With Formulas, Fraphs, and Mathematical Tables*. 1964.

[18] M. Wright, *Nanoparticle Tracking Analysis for the Multiparameter Characterization and Counting of Nanoparticle Suspensions*, ch. 41, pp. 511–524. Totowa, NJ: Humana Press, 2012.

[19] B. Carr and M. Wright, "Nanoparticle tracking analysis," *Innovations in Pharmaceutical Technology*, vol. 26, pp. 38–40, 2008.

[20] K. Miller, R. Erez, E. Segal, D. Shabat, and R. Satchi-Fainaro, "Targeting bone metastases with a bispecific anticancer and antiangiogenic polymer–alendronate–taxane conjugate," *Angewandte Chemie International Edition*, vol. 48, no. 16, pp. 2949–2954, 2009.

[21] R. Krishnamurthy, M. Sukumar, T. Das, and N. Lacher, "Emerging analytical technologies for biotherapeutics development," *Bioprocess Int*, vol. 6, pp. 32–42, 01 2008.

[22] S. Du, K. Kendall, S. Morris, and C. Sweet, "Measuring number concentrations of nanoparticles and viruses in liquids on line. shangfeng du, kevin kendall, susan morris and clive sweet," *Journal of Chemical Technology & Biotechnology*, pp. 1223–1228, 09 2010.

[23] Y. Gu, W. Ha, A. E. Augspurger, K. Chen, and N. Fang, "Single Particle Orientation and Rotational Tracking (SPORT) in biophysical studies," *Nanoscale*, vol. 5, no. 22, 2013.

[24] A. S. Stender, K. Marchuk, C. Liu, S. Sander, M. W. Meyer, E. A. Smith, B. Neupane, G. Wang, J. Li, J.-X. Cheng, B. Huang, and N. Fang, "Single cell optical imaging and spectroscopy," *Chemical reviews*, vol. 113, pp. 2469–2527, apr 2013.

[25] G. Wang, W. Sun, Y. Luo, and N. Fang, "Resolving Rotational Motions of Nano-objects in Engineered Environments and Live Cells with Gold Nanorods and Differential Interference Contrast Microscopy," *Journal of the American Chemical Society*, vol. 132, no. 46, pp. 16417–16422, 2010.

[26] R. Pecora, *Dynamic Light Scattering: Applications of Photon Correlation Spectroscopy*. New York: Plenum Press, 1 ed., 1985.

[27] J. N.C.Ford, "Light Scattering Apparatus," in *Dynamic Light Scattering: Applications of Photon Correlation Spectroscopy* (R. Pecora, ed.), ch. 2, pp. 7–57, New York: Plenum Press, 1 ed., 1985.

[28] L. Brillouin, "Diffusion de la lumière par un corps transparent homogène," *CR. Acad Sci.*, vol. 158, pp. 1331–1334, 1914.

[29] K. Zero and R. Pecora, "Dynamic Depolarized Light Scattering," in *Dynamic Light Scattering: Applications of Photon Correlation Spectroscopy* (R. Pecora, ed.), ch. 3, pp. 59–81, New York: Plenum Press, 1 ed., 185.

[30] B. J. Berne and R. Pecora, *Dynamic Light Scattering with Application to Chemistry, Biology and Physics*. New York: Dover Publications, Inc., 1976.

[31] S. R. S. Aragón and R. Pecora, "Anisotropic light scattering from phospholipid vesicles," *Journal of Colloid and Interface Science*, vol. 89, no. 1, pp. 170–184, 1982.

[32] M. I. Mishchenko, L. D. Travis, and D. W. Mackowski, "T-Matrix Codes for Computing Electromagnetic Scattering by Nonspherical and Aggregated Particles."

[33] M. I. Mishchenko and L. D. Travis, "T-matrix computations of light scattering by nonspherical particles: A review," *Journal of Quantitative Spectroscopy and Radiative Transfer*, vol. 55, no. 5, pp. 535–575, 1996.

[34] M. I. Mishchenko and L. D. Travis, "Capabilities and Limitations of a Current Method for Randomly Oriented , Rotationally Symmetric Scatterers," *J. Quant. Spectrosc. Radiat. Transfer*, vol. 60, no. 3, pp. 309–324, 1998.

[35] M. I. Mishchenko, "Calculation of the amplitude matrix for a nonspherical particle in a fixed orientation," *Applied Optics*, vol. 39, no. 6, pp. 1026–1031, 2000.

[36] J. Leinonen, "pytmatrix." *Available at* https://github.com/jleinonen/pytmatrix.

[37] S. Asano and G. Yamamoto, "Light Scattering by a Spheroidal Particle," *Applied Optics*, vol. 14, no. 1, pp. 29–49, 1975.

[38] P. Török, P. D. Higdon, and T. Wilson, "Theory for confocal and conventional microscopes imaging small dielectric scatterers," *Journal of Modern Optics*, vol. 45, no. 8, pp. 1681–1698, 1998.

[39] P. Török, P. Varga, Z. Laczik., and G. R. Booker, "Electromagnetic diffraction of light focused through a planar interface between materials of mismatched refractive indices : an integral representation," *J. Opt. Soc. Am. A*, vol. 12, no. 2, pp. 325–332, 1995.